Electronic Supplementary Material (ESI) for Energy & Environmental Science.

Electronic Supporting Information

Helical Cobalt Borophosphates Master Durable Overall Water-Splitting

Prashanth W. Menezes,* Arindam Indra, Ivelina Zaharieva,* Carsten Walter, Stefan Loos, Stefan Hoffmann, Robert Schlögl, Holger Dau*, Matthias Driess*

[a] Department of Chemistry: Metalorganics and Inorganic Materials, Technische Universität Berlin, Straße des 17 Juni 135, Sekr. C2, 10623 Berlin, Germany

[b] Fachbereich Physik, Freie Universität Berlin, Arnimallee 14, 14195 Berlin, Germany

[c] Fritz Haber Institute of the Max Planck Society, Faradayweg 4–6, 14195 Berlin, Germany

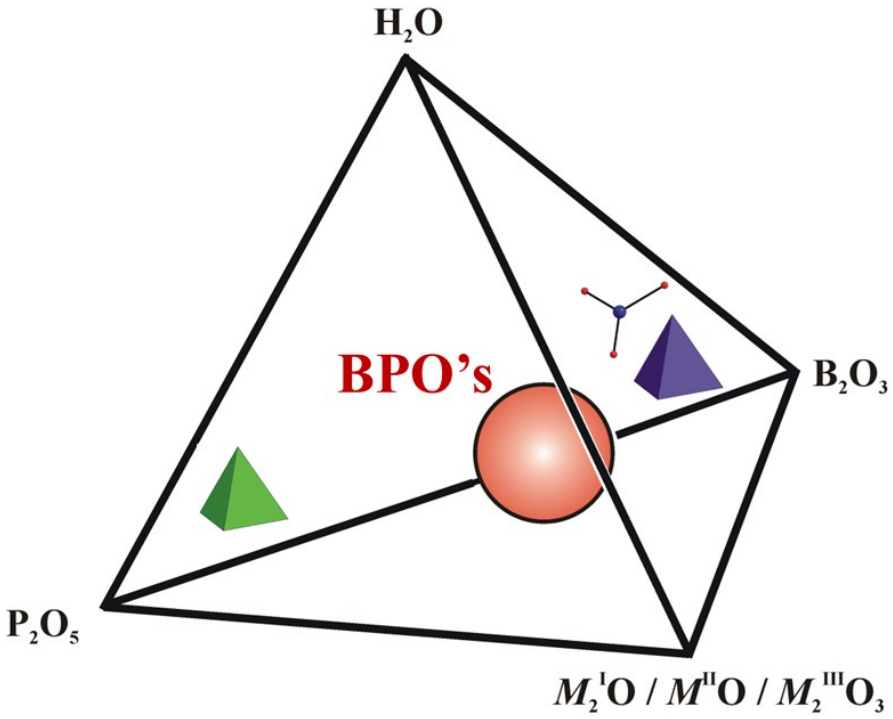

Fig. S1. Schematic representation of borophosphates (BPO's, schematically by the red ball), which are intermediate compounds of systems M_xO_y–B_2O_3–P_2O_5–(H_2O) (M = main group or transition metal).[1,2] The complex anionic structures of BPO's are comprised of interconnected trigonal–planar BO_3 (ball and stick) and/or BO_4 (blue tetrahedron) and PO_4 (green tetrahedron) groups and their partially protonated species. The classification of BPO's is entirely focused on the anionic partial structures, although it is clear that the cations (charge, size, and coordination behavior) have a substantial impact even on the dimensionality of the anionic structural units. In principle, the BPO's are broadly divided into five groups as follows. 1) **Tetrahedral**, which comprises of anionic arrangements that contain solely BO_4 and PO_4 tetrahedra and no trigonal–planar borate group BO_3 unit (helical BPO's belong to this group), 2) **Mixed–coordinated**, that contain a BO_3, and/or BO_4 and PO_4, 3) **Metallo-,** contains a 3D network structure composed of BO_4, PO_4, and MO_4 tetrahedra (M = metal), 4) **Anion–substituted,** where the oxoligands of the complex anions are substituted (such as fluorine substituted), and 5) **Borate–phosphates** with isolated borate (BO_3, BO_4) and phosphate (PO_4) groups.[3-8]

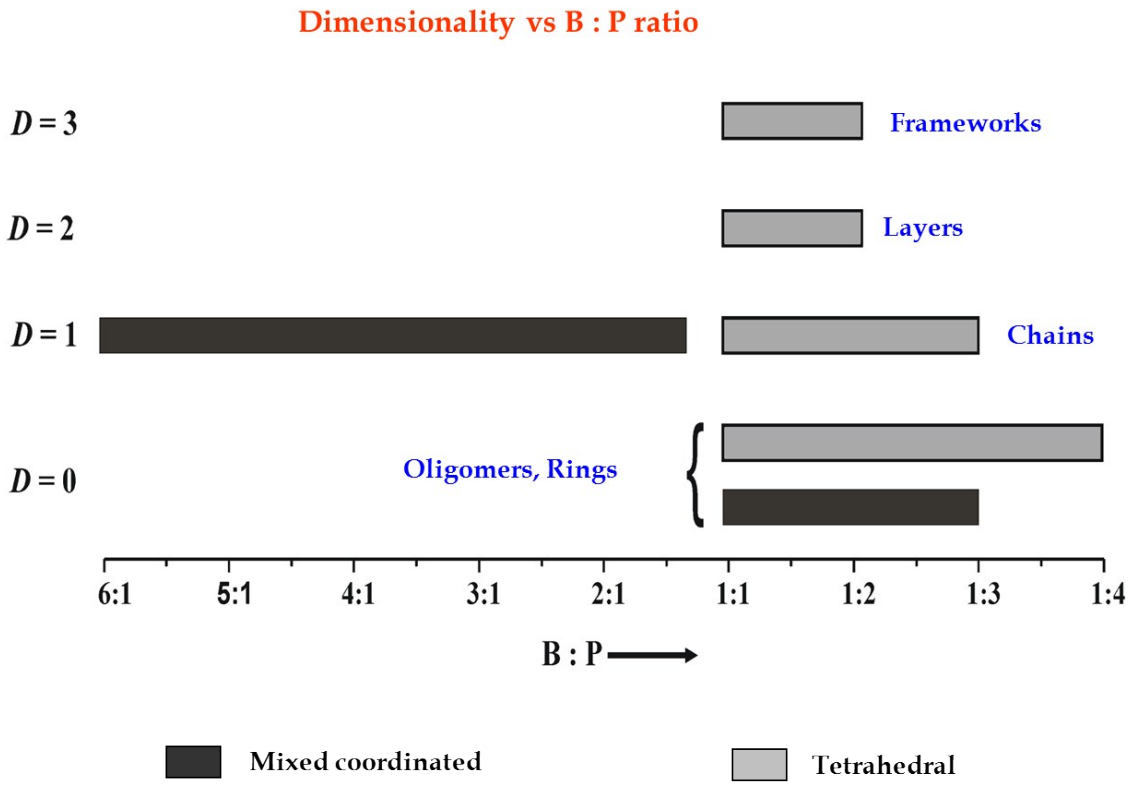

Fig. S2. BPO's exclusively linked via common corners to form isolated species, oligomers, rings, chains, layers, and even frameworks. Dimensionality of complex BPO's anionic partial structures; mixed coordinated (dark grey) and tetrahedral (light grey) BPO's are shown in the Figure. Layers and frameworks (D = 2 – 3) are detected with compositions between B:P = 1:1 and 1:2. The oligomers, rings, and chains are known within the composition range from B:P = 6:1 to 1:4.[1,2,7] The presented BPO's falls in the category of D = 1; B:P = 1:2.

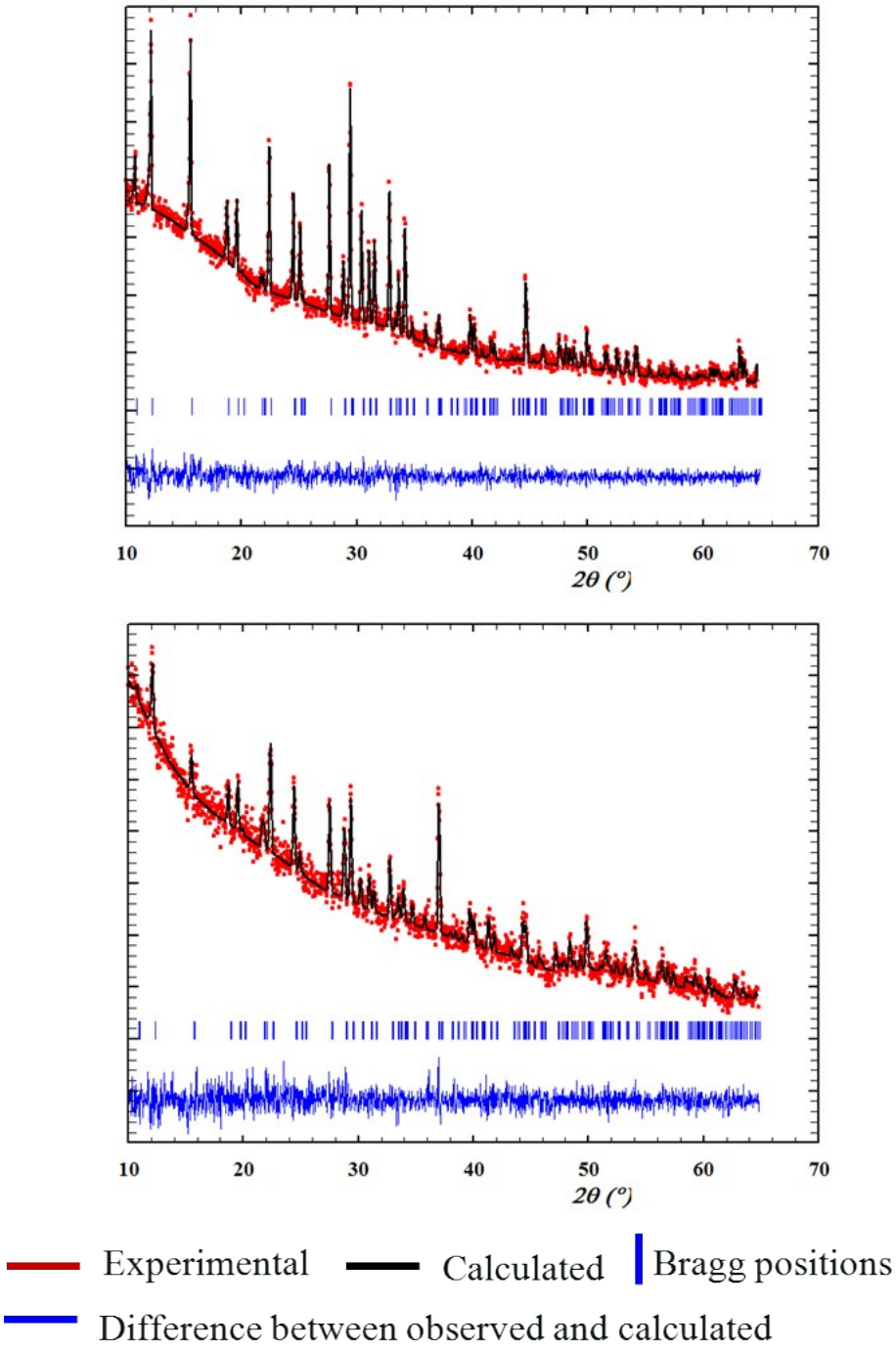

Fig. S3. Rietveld refinement patterns of high-resolution PXRD of the (top) $LiCo(H_2O)_2[BP_2O_8]\cdot H_2O$ (**LiCoBPO**) and (bottom) $NaCo(H_2O)_2[BP_2O_8]\cdot H_2O$ (**NaCoBPO**). Red dots: experimental data points; black line: calculated powder pattern; blue ticks: Bragg positions; blue line: the difference between the observed and calculated patterns.[9,10]

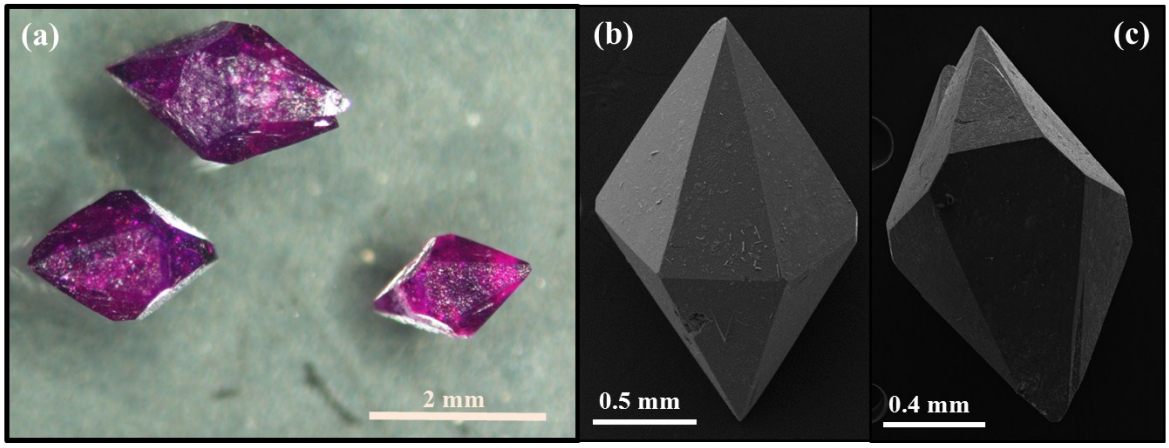

Fig. S4. Optical microscopic (a) and SEM images (b, c) of the single crystals of **LiCoBPO**. From the images, it was observed that well-defined pink crystals of hexagonal bipyramids with definite shape and facets were produced. The dimensions of the single crystals varied ranging from 0.1 mm to 0.5 mm.

Chemicals

All chemical reagents (analytical grade) were used as received without any further purification. Deionized water was used to carry out all the experiments. Commercially available cobalt(II) acetate tetrahydrate ($Co(CH_3COO)_2 \cdot 4H_2O$), lithium tetraborate ($Li_2B_4O_7$), sodium tetraborate ($Na_2B_4O_7$), phosphoric acid ($H_3PO_4$, 85%), sodium phosphate tribasic dodecahydrate ($Na_3PO_4 \cdot 12H_2O$), potassium hydroxide (1 M KOH, Fe < 0.05 ppm determined by ICP-AES) were obtained from Sigma Aldrich whereas ruthenium oxide (RuO_2) and iridium oxide (IrO_2), cobalt hydroxide ($Co(OH)_2$), cobalt oxide (Co_3O_4) metallic Co was purchased from Alfa Aesar.

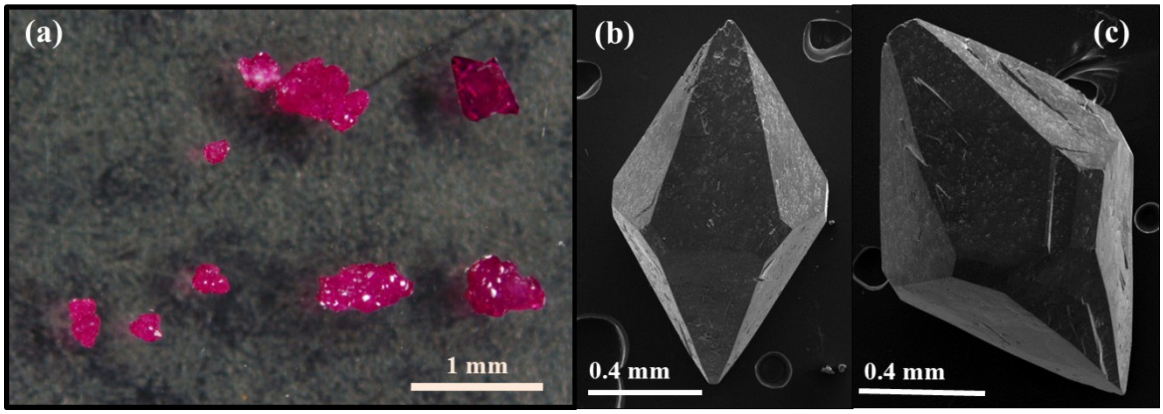

Fig. S5. Optical microscopic (a) and SEM images (b, c) of the single crystals of **NaCoBPO**. Although similar to **LiCoBPO**, well-defined pink crystals of hexagonal bipyramids with definite shape were produced, however, the roughness of the facets as well as the formation of additional facets at the edges was also found. The dimensions of the single crystals varied between 0.1 mm to 0.5 mm.

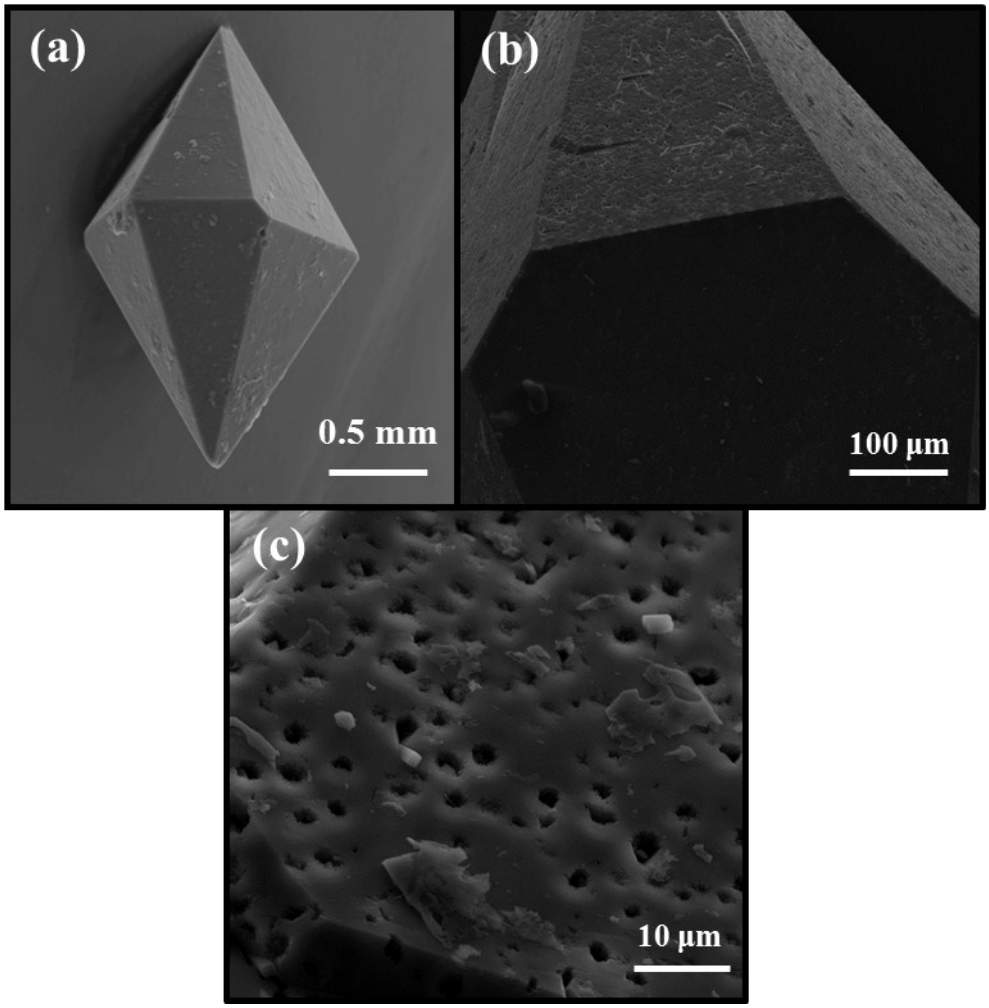

Fig. S6. SEM (a), and high resolution (HR) SEM images (b, c) of the single crystals of **LiCoBPO**. Interestingly, the hexagonal bipyramids were porous in nature and the pore sizes of each pore were approximately 1400 nm (see Fig. 1, main text)

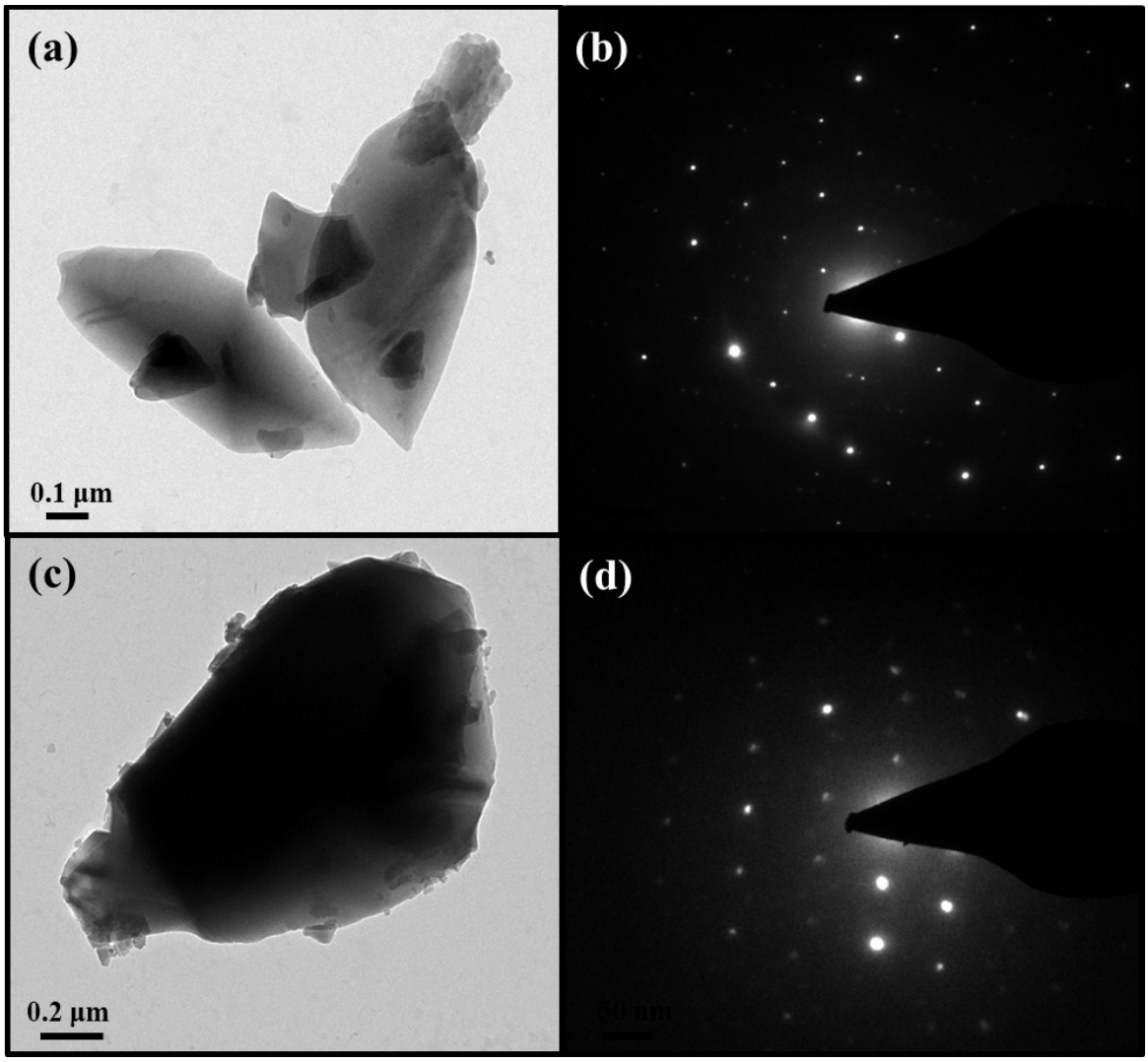

Fig. S7. TEM images (a, c) and the corresponding selected area electron diffraction (SAED) (b, d) patterns of the ground crystals of **LiCoBPO** and the **NaCoBPO**. The crystals were well crystalline and also quite large in size.

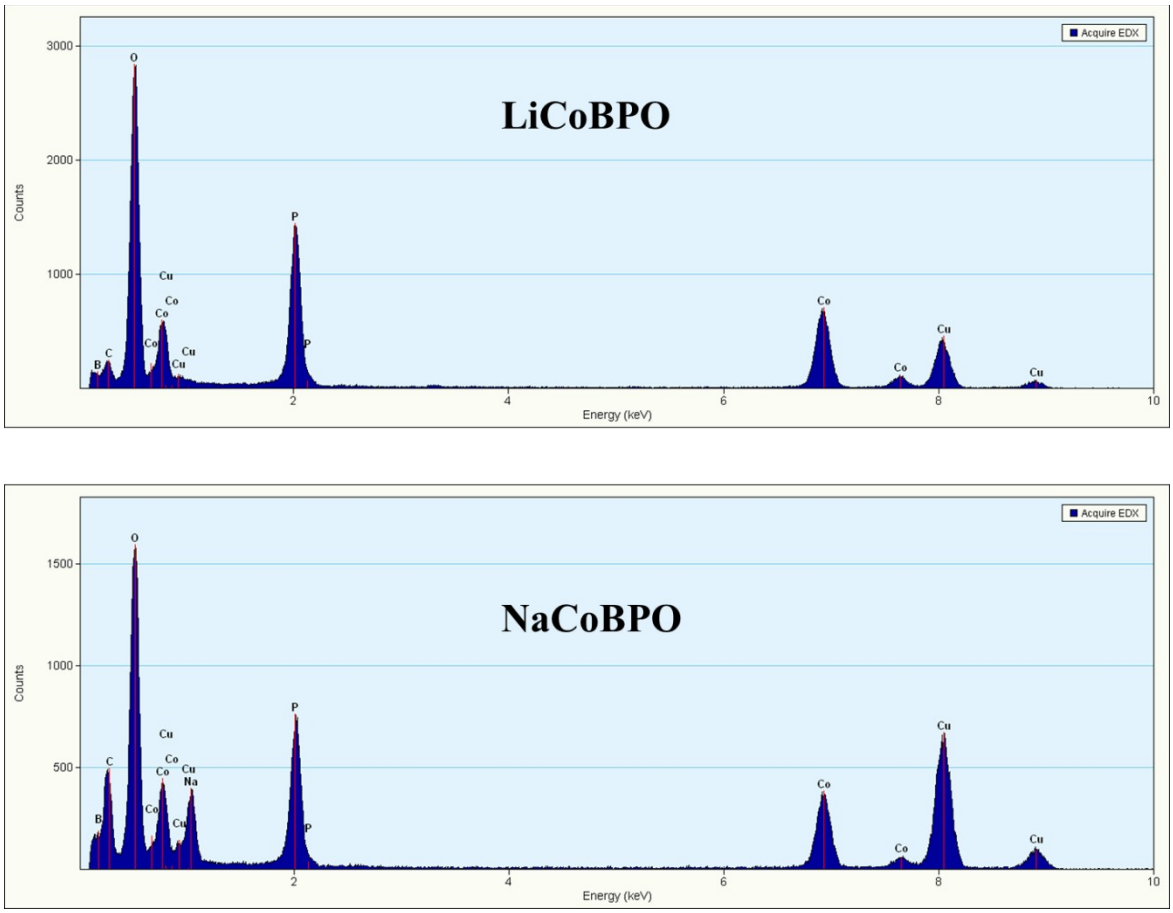

Fig. S8. The presence of cobalt and phosphorous in **LiCoBPO** (top) and **NaCoBPO** (bottom) were determined by the EDX. The appearance of peaks for carbon and copper is due to TEM grid (carbon film on 300 mesh Cu-grid).

Table S1. Determination of chemical composition in **LiCoBPO** and **NaCoBPO** was obtained by EDX, XPS and ICP-AES analysis.

	Li/Na:Co:B:P (Theo.)	Co:P (EDX)	Li/Na:Co:B:P (XPS)	Li/Na:Co:B:P (ICP-AES)
$LiCo(H_2O)_2[BP_2O_8]\cdot H_2O$ (**LiCoBPO**)	1:1:1:2	~1:2.08	1:1.04:0.94:2.1	1:1:1:2
$NaCo(H_2O)_2[BP_2O_8]\cdot H_2O$ (**NaCoBPO**)	1:1:1:2	~1:2.1	1:1.1:0.91:2.03	1:1:1:2

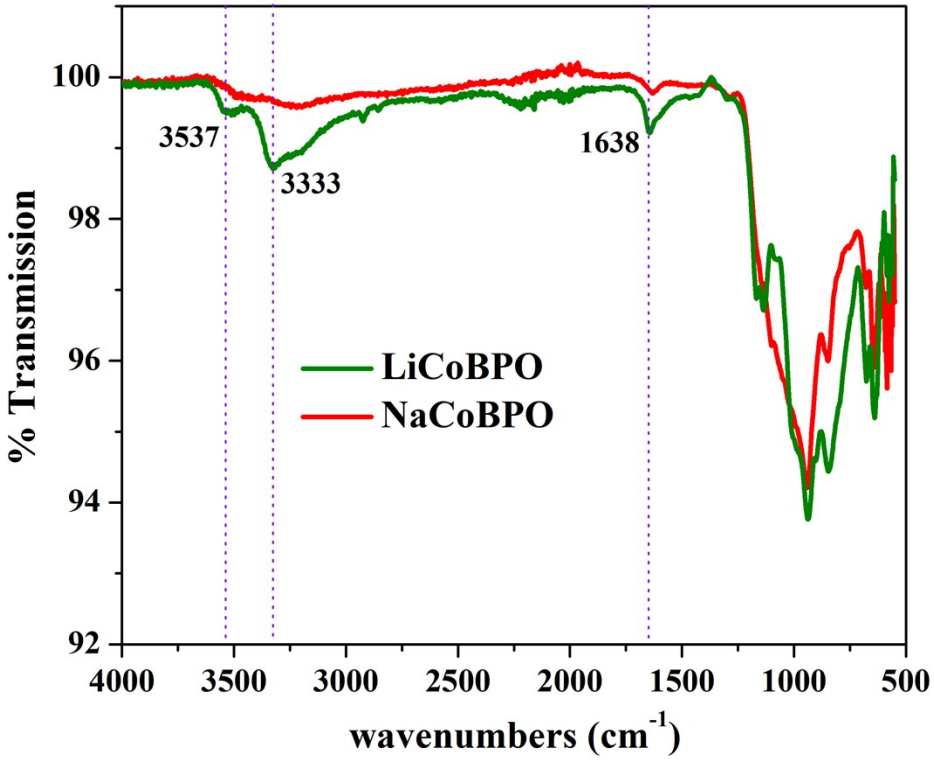

Fig. S9. IR spectra of **LiCoBPO** and **NaCoBPO** show the presence of water by characteristic absorption bands at about ~1638 cm^{-1} (H_2O deformation) and between 3000 and 3600 cm^{-1} (O–H stretching). In addition to this, the spectrum in each case is dominated by the strong P−O stretching modes in the region ranging from 800 to 1100 cm^{-1} and overlaps heavily with the strong B−O stretching vibrations in the range of 700−1200 cm^{-1}.[7,10,11]

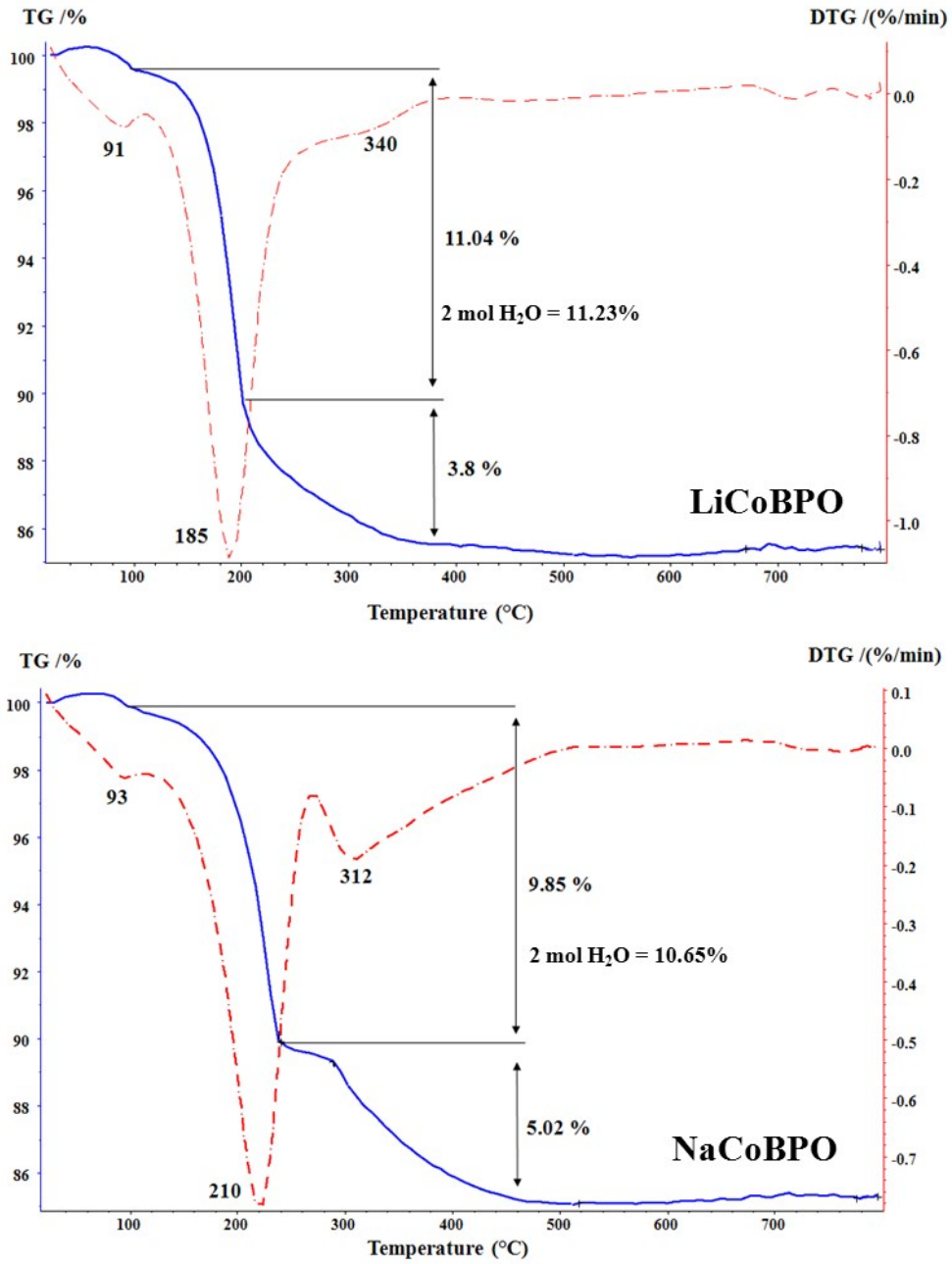

Fig. S10. TGA (blue solid line) and its differential (DTG, red dotted line) plot of the materials thermally treated from room temperature to 800 ˚C in a nitrogen atmosphere at the rate of 5 K/min. The dehydration of both **LiCoBPO** and **NaCoBPO** were a two-step process between 100–230 ºC and the mass loss corresponds to a distinct DTG peak at 185 and 210 ˚C. The experimental mass loss (11.04 and 9.85%) obtained in both cases were consistent with the calculated weight (11.23 and 10.65%) of two water molecules per formula unit. The second mass loss occurred at 240 to 480 ˚C with a DTG peak at 320 and 312 ˚C. The mass loss within this step was also very close to the calculated value of the release of the third water molecule evidencing the formation of the pure phase of BPOs.[7]

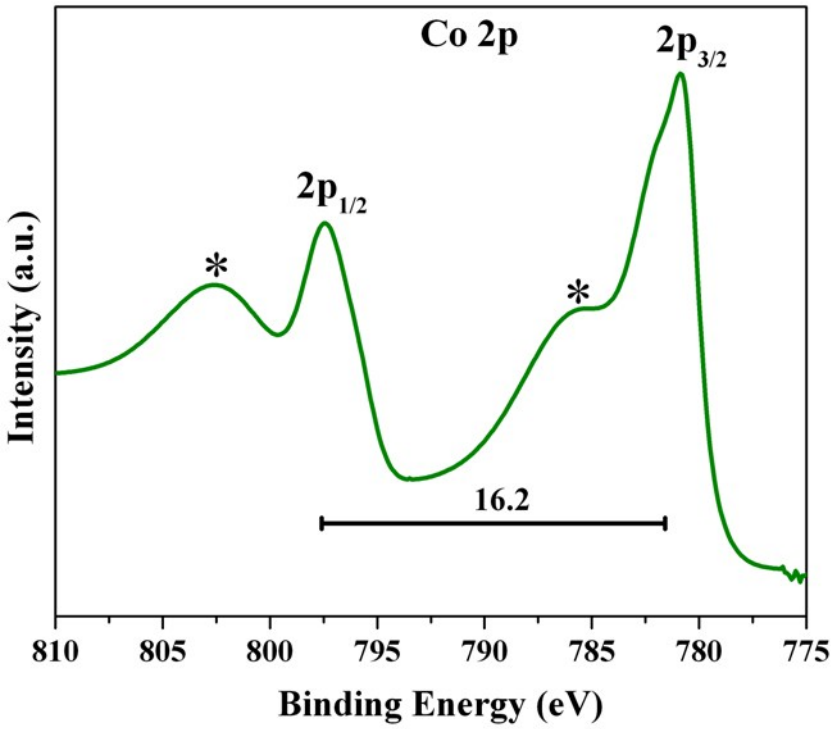

Fig. S11 High-resolution Co 2p XPS spectra of **LiCoBPO**. The Co(II) and Co(III) have almost similar 2p binding energies but can be differentiated by the Co $2p_{1/2}$−$2p_{3/2}$ spin−orbit level energy spacing which is 16 eV for Co(II) and 15 eV for Co(III).[12-14] The spacing of 16.2 eV and the typical satellite peaks (*) attained here is consistent with the presence of Co(II).[15-18]

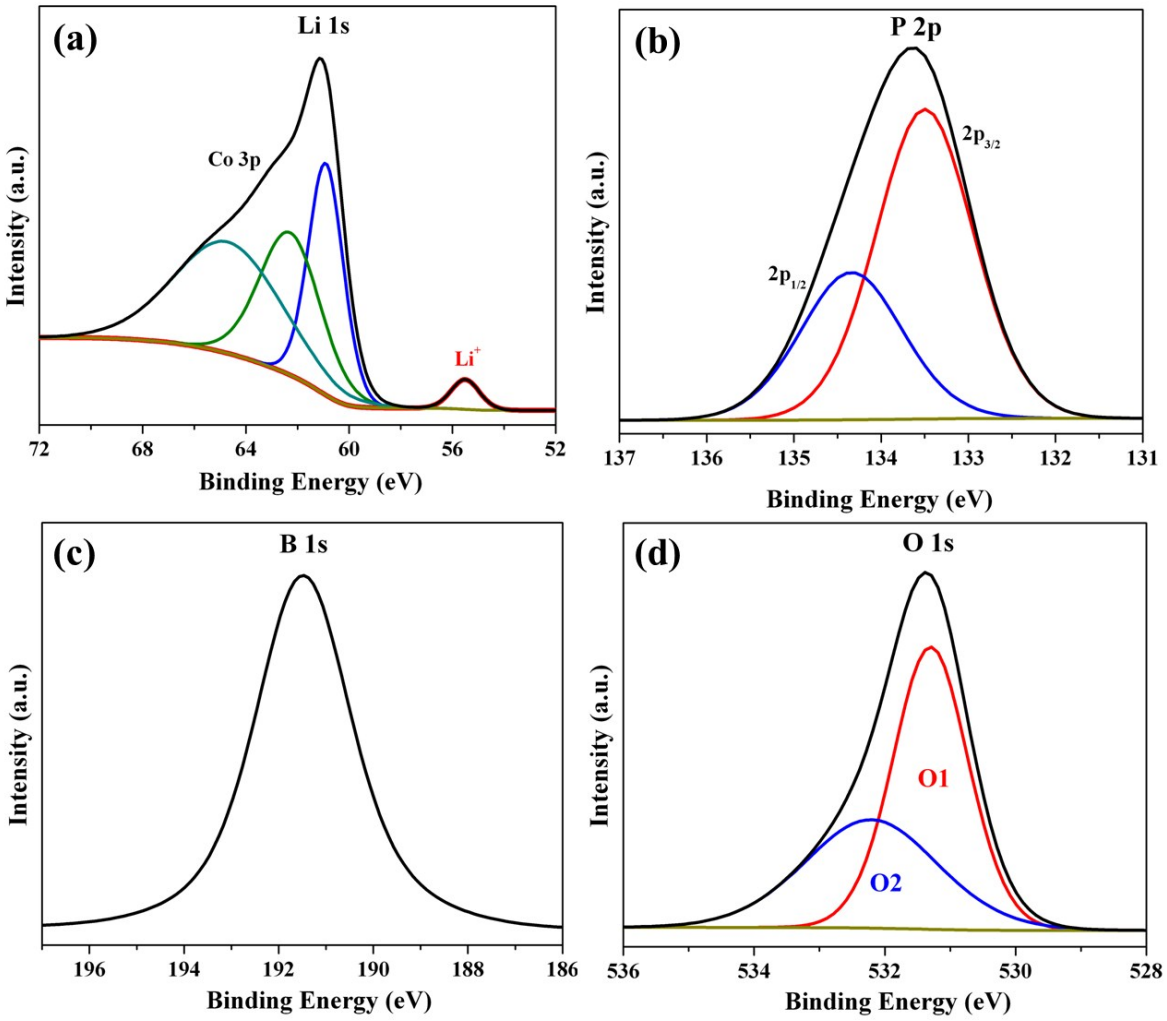

Fig. S12. Typical high-resolution XPS spectra of the regions containing the (a) Li 1s (b) P 2p, (c) B 1s and (d) O1s of as-synthesized **LiCoBPO**. The Li 1s binding energy peaks at 55.5 eV alongside with the broad Co 3p peak at approximately 62 eV and could be directly compared to the other Li^+ compounds.[19,20] In the case of P 2p, the appearance of the peaks at 133.5 and 134.3 eV, corresponds to $2p_{3/2}$ and $2p_{1/2}$ that are attributed to the formation of phosphate $(PO_4)^{3-}$ on the surface which is in good agreement with the literature reported phosphate materials.[21-23] The B 1s XPS spectrum exhibited a peak at ~191.4 eV is attributed to the structure of boron linked to oxygen atoms with four coordination indicative of B^{3+}(borate).[24-26] The O 1s spectrum was deconvoluted into broad O1 and O2 peaks. The peak at ~531.4 eV (O1) is due to the large dominance of –OH species adsorbed on the surface by surface hydroxides. The O2 peak ~532.6 eV (O1) could be assigned to the chemisorbed oxygen or associated crystal water in the structure. The O1s values obtained here can be well matched with literature reported materials of phosphates and borates.[21,22,26]

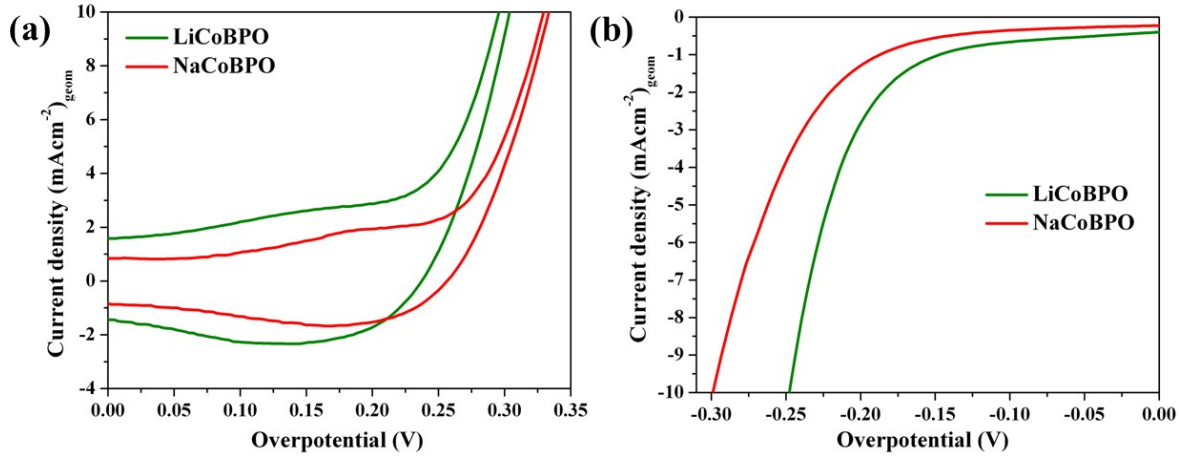

Fig. S13. (a) OER CV and (b) HER LSV of **LiCoBPO** and **NaCoBPO** at a sweep rate 5 mV/s of in 1 M KOH electrolyte. The overpotential for the OER (a) was determined to be 293 mV at a current density of 10 $mAcm^{-2}$ for the **LiCoBPO,** whereas 328 mV was obtained for the **NaCoBPO**. From the shape of the CVs between 0 and 0.25 V overpotential, it is also evident that a higher amount of Co^{3+} exists on the inner and outer surfaces of **LiCoBPO** compared to **NaCoBPO**. This Co^{3+} can serve as the catalytically active site for the OER for both catalysts.[15-17,27] The overpotential determined for HER at -10 $mAcm^{-2}$ was 245 mV for **LiCoBPO** and 298 mV for **NaCoBPO**.

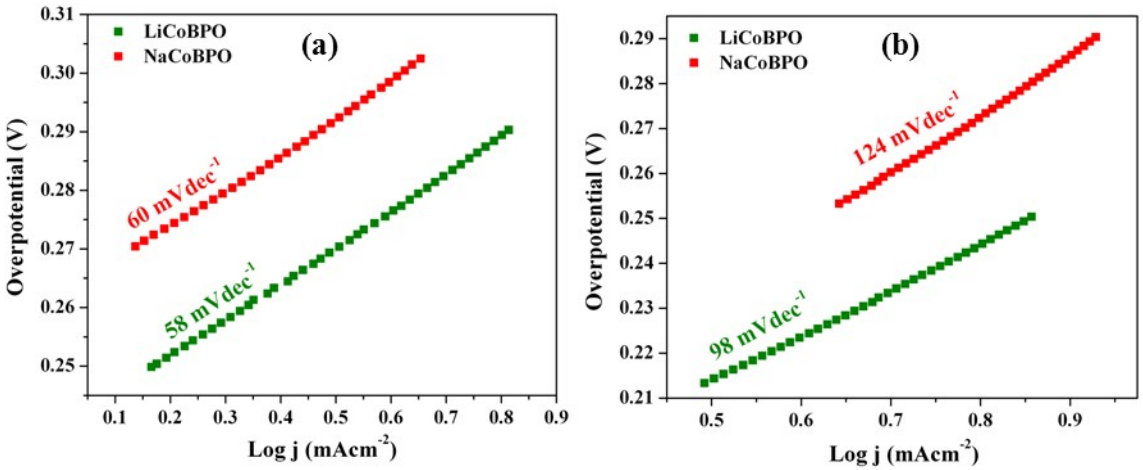

Fig. S14. Tafel slopes derived for (a) OER and (b) HER from the polarization curves at 1 mV/s on FTO in 1 M KOH solution. A Tafel slope of 58 $mVdec^{-1}$ was obtained for **LiCoBPO** whereas a slope of 60 $mVdec^{-1}$ was recorded for **NaCoBPO** in OER corresponding to more favorable OER kinetics. Similarly, in HER, the Tafel slope of **LiCoBPO** was 98 $mVdec^{-1}$, smaller than that of **NaCoBPO** (124 $mVdec^{-1}$), indicating the more facile reaction of **LiCoBPO**.

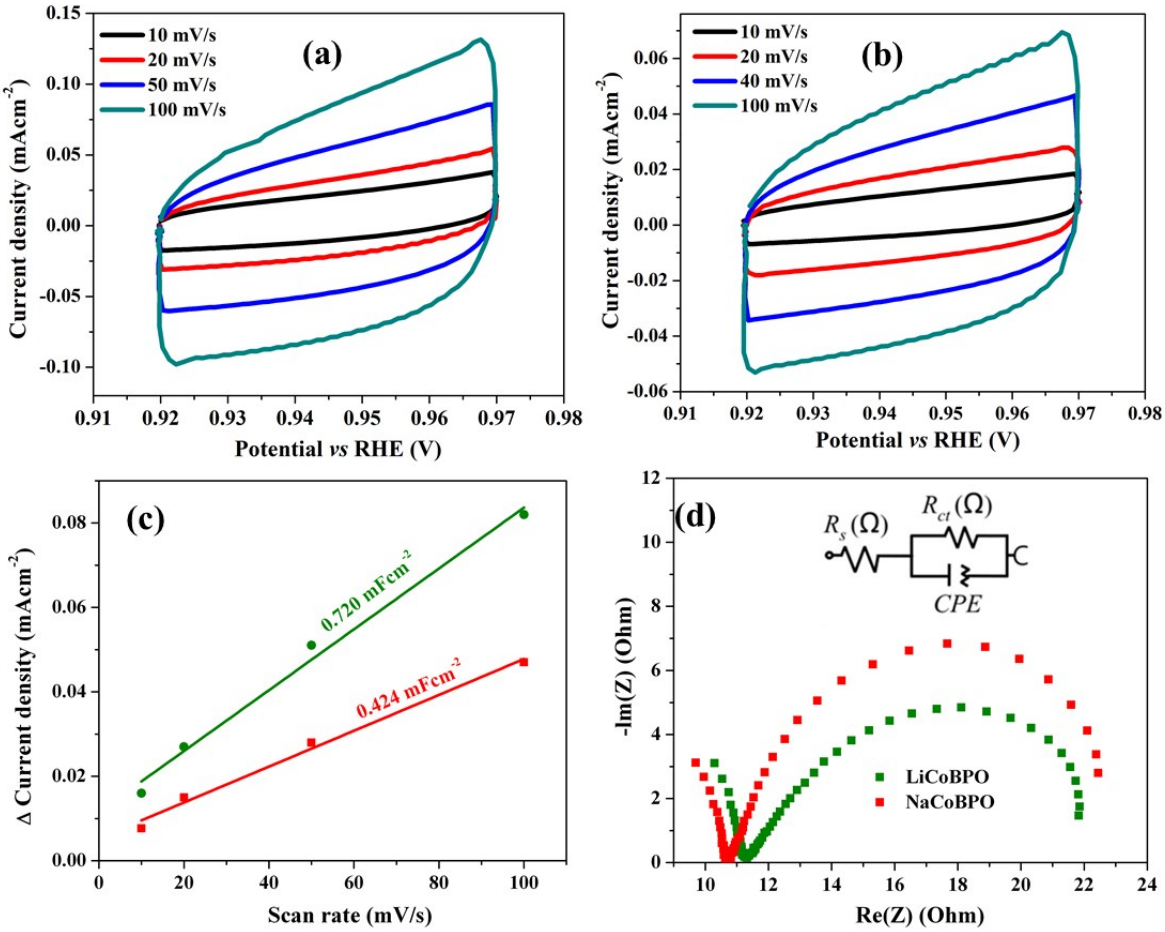

Fig. S15. Electrochemical capacitance measurements for the estimation of the relative electrochemical active surface area (ECSA) in a non-Faradaic potential range of 0.92 V to 0.97 V vs RHE at different scan rates (10, 20, 50, 100 mV/s) for (a) **LiCoBPO** and (b) **NaCoBPO** on FTO in 1 M KOH electrolyte. (c) Estimation of double-layer capacitances (C_{dl}) by plotting the current density variation ($\Delta j = (j_a - j_c)/2$), obtained from the (a) and (b) at 0.945 V vs RHE.[28,29] Nyquist plots (d) obtained from electrochemical impedance spectroscopy (EIS) for **LiCoBPO** and **NaCoBPO**. The spectra were collected with an anodic polarization potential of 1.55 V vs RHE. The curves were fitted by the inserted Randles equivalent circuit, where R_s, CPE, and R_{ct} are the equivalent series resistance, constant phase element of the double-layer capacitance, and the charge transfer resistance, respectively.[28]

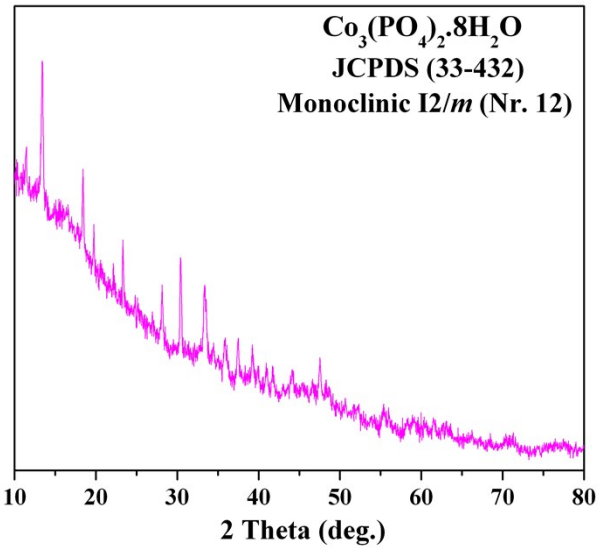

Fig. S16. The PXRD pattern of as-synthesized cobalt phosphate (see Experimental). The obtained compound could be well matched with $Co_3(PO_4)_2 \cdot 8H_2O$ that crystallizes in the monoclinic system. The cobalt phosphate was synthesized in order to have a direct comparison of the activity with the cobalt BPO catalysts.

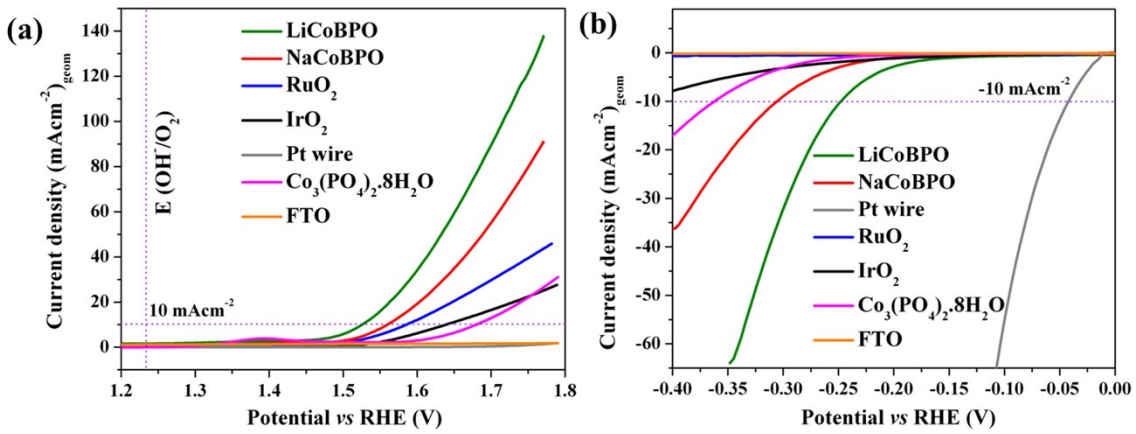

Fig. S17. Comparison of (a) OER LSV and (b) HER LSV of **LiCoBPO** and **NaCoBPO** with noble commercial benchmark and as-synthesized CoPi catalysts at a sweep rate 5 mV/s in 1 M KOH electrolyte. The **LiCoBPO** was found to be highly active for OER resulting into lower overpotential in comparison to **NaCoBPO** and also surpassed the activity significantly than the RuO_2, IrO_2, and $Co_3(PO_4)_2 \cdot 8H_2O$ catalysts. The Pt was found to be inactive for OER within the measured range. On the other hand, Pt was extremely active for HER in comparison to **LiCoBPO** and **NaCoBPO**. The other commercial and $Co_3(PO_4)_2 \cdot 8H_2O$ catalyst was clearly less active for HER (see Table S4 for overpotentials).

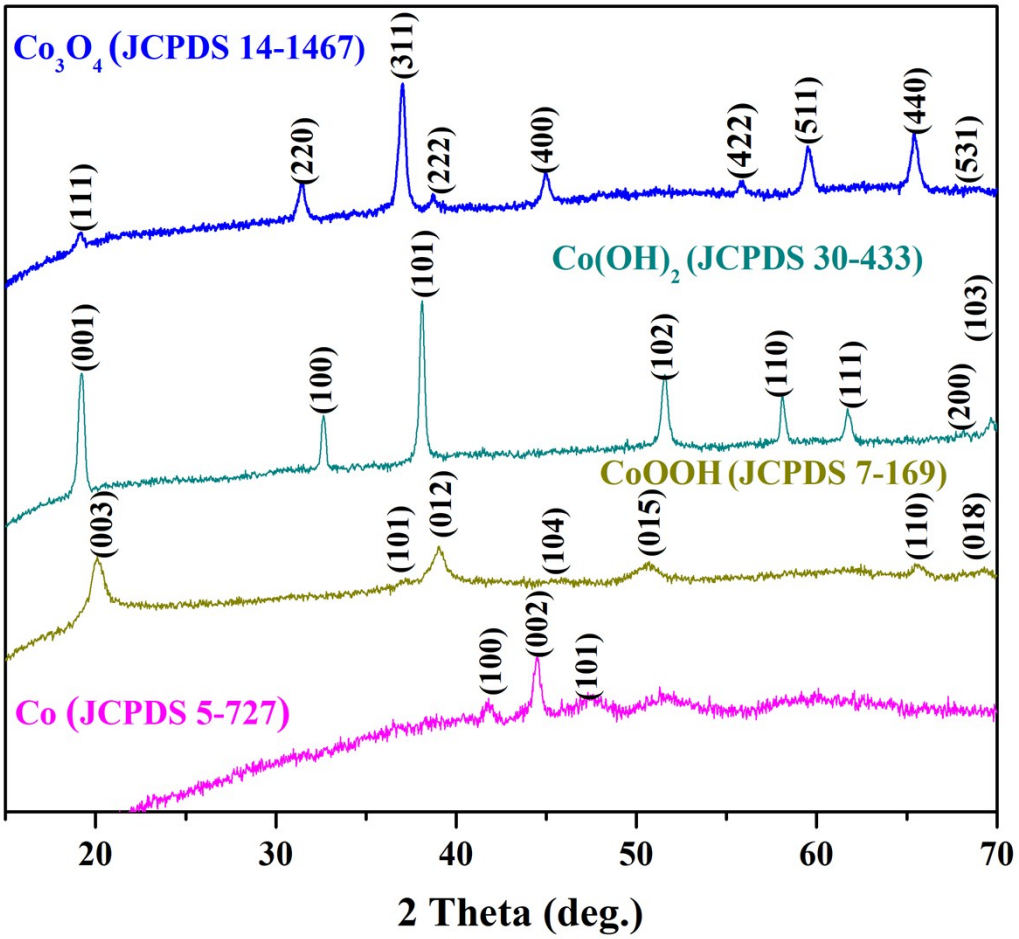

Fig. S18. PXRD of Co_3O_4 (JCPDS 14-1467), $Co(OH)_2$ (JCPDS 30-433), CoOOH (JCPDS 7-169) and the metallic Co (JCPDS 5-727) nanoparticles that were used as references for evaluating the catalytic OER and HER activities of **LiCoBPO** and **NaCoBPO**.

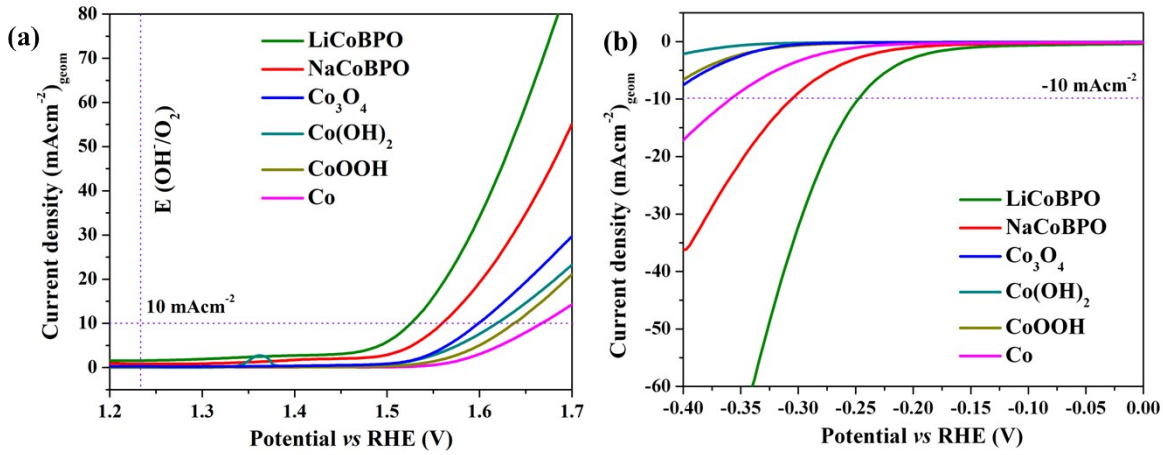

Fig. S19. Comparison of (a) OER and (b) HER polarization curves of **LiCoBPO** and **NaCoBPO** with the Co_3O_4, $Co(OH)_2$, CoOOH and the metallic Co catalysts on FTO substrates at a sweep rate 5 mV/s in 1 M KOH electrolyte. For OER, the overpotential of Co_3O_4, $Co(OH)_2$, CoOOH and Co catalysts at 10 $mAcm^{-2}$ was 360, 382, 401 and 430 mV whereas only metallic Co could reach the current density of -10 $mAcm^{-2}$ reaching an overpotential of 315 mV for HER. The attained overpotentials were significantly lower compared to the **LiCoBPO** catalyst (see Table S4).

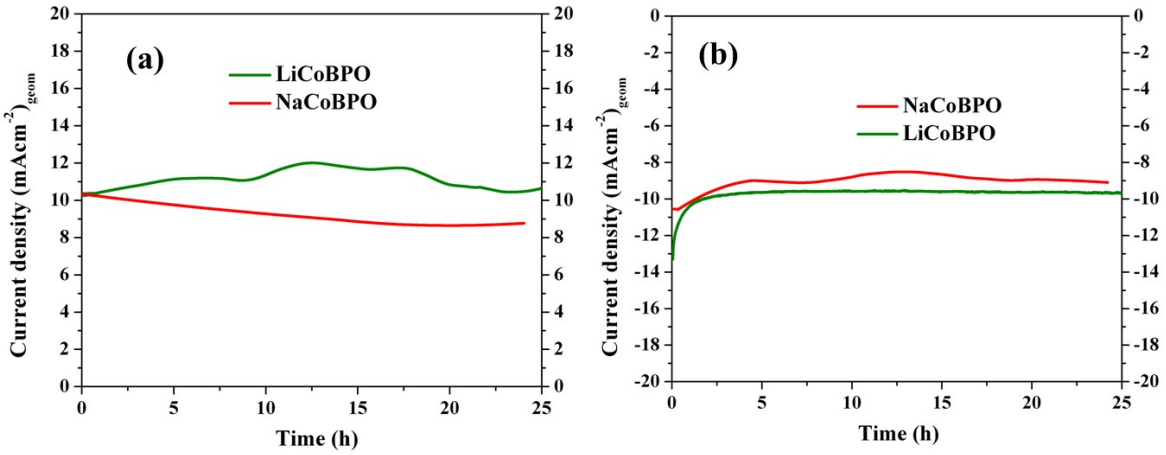

Fig. S20. The chronoamperometric (CA) results of **LiCoBPO** and **NaCoBPO** measured under OER conditions (a) at 1.53 and 1.56 V vs RHE maintaining at 10 $mAcm^{-2}$ in 1 M KOH solution. The **LiCoBPO** catalyst was stable for more than 24 hours and a moderate decrease in the activity for **NaCoBPO** was observed. The CA responses of **LiCoBPO** and **NaCoBPO** for HER (b) were measured at -0.25 and -0.3 V vs RHE (at -10 $mAcm^{-2}$). Similar to the OER CA, **LiCoBPO** was highly stable under HER CA conditions and was better than that of **NaCoBPO**.

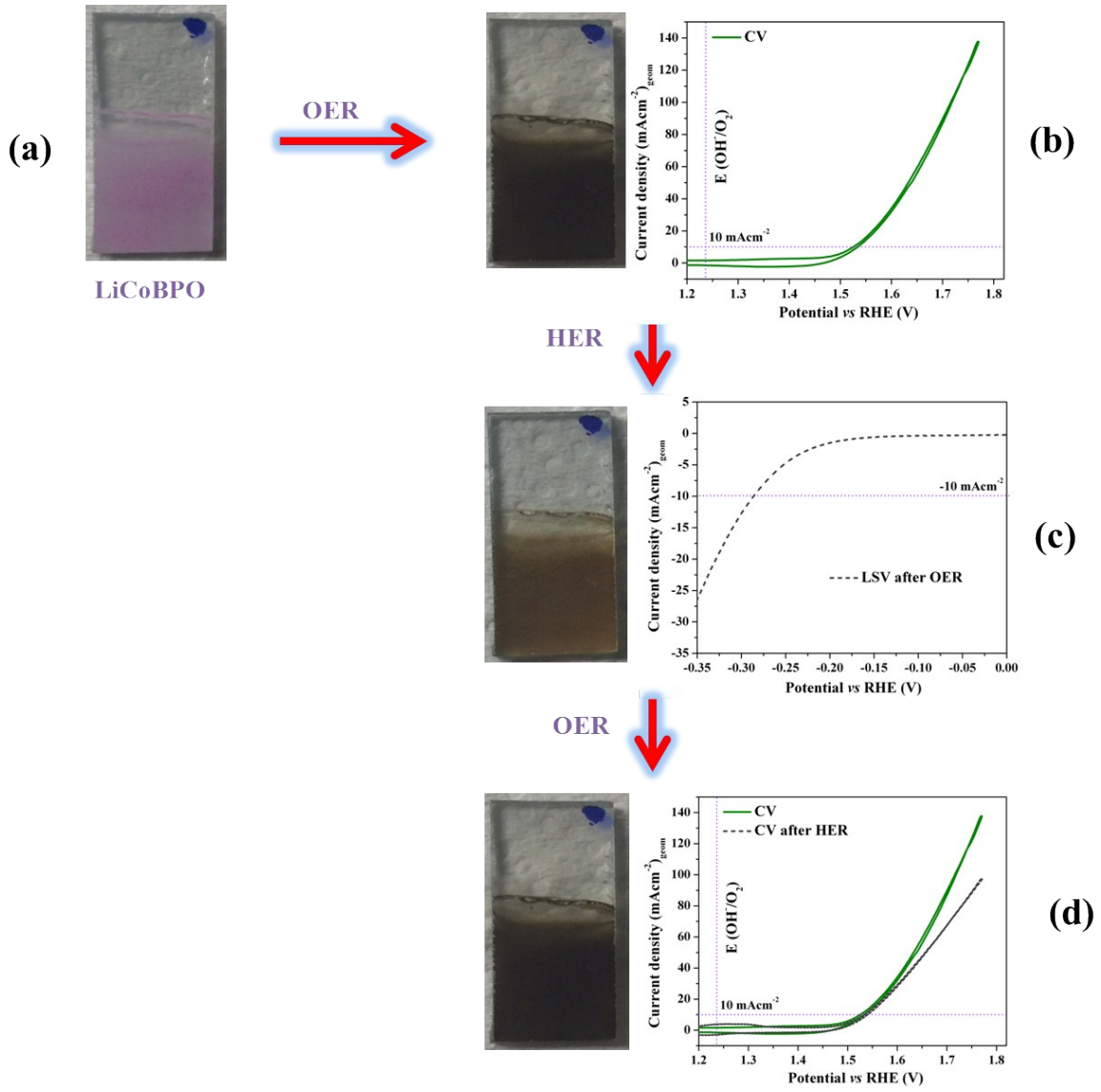

Fig. S21. The switchable properties during OER for **LiCoBPO** were measured using electrochemical conditions using 1 M KOH in a three-electrode setup. First, the pinkish FTO film (a) was subjected to OER CV (overpotential ~293 mV at 10 $mAcm^{-2}$) to form a black film (b) showing immediate structural changes and subsequently, OER CA was performed for 2 h at 1.53 V vs RHE. After the OER CA, the black film was examined for HER LSV (c) forming a light brown colored film (overpotential -285 mV at -10 $mAcm^{-2}$) which was then maintained for HER CA for 2 h at -0.28 V vs RHE. Remarkably, when the light brown films were further scanned for OER CV, the reversibility of the catalytic performance (d), as well as the change in color back to black, was observed. The difference in the overpotentials for the first OER CV (b) as well as the OER CV after HER (d) was observed to be negligible at 10 $mAcm^{-2}$ whereas HER LSV (c) exhibited less activity than first HER LSV (see Fig. 2b).

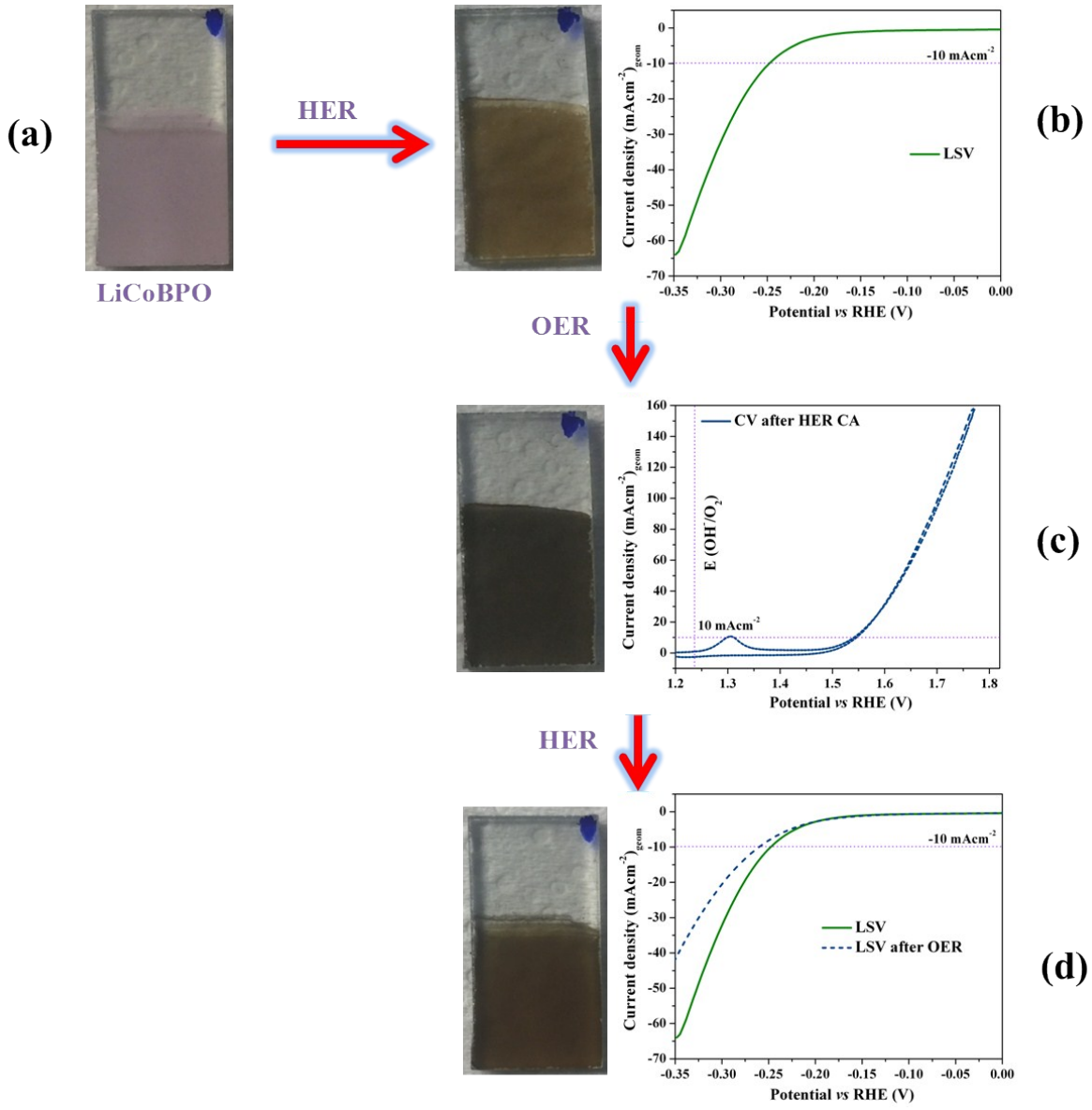

Fig. S22. The switchable properties for HER for **LiCoBPO** were measured under electrochemical conditions using 1 M KOH in a three-electrode setup. Foremost, the pinkish FTO film (a) was subjected to HER LSV (overpotential ~-245 mV at -10 mAcm^{-2}) to form a light brown colored film (b) showing immediate structural changes and subsequently, HER CA was performed for 2 h at -0.25 V vs RHE. After the HER CA, the light brown film was examined for OER (c) forming a black colored film (overpotential ~300 mV at 10 mAcm^{-2}) which was then maintained for OER CA for 2 h at 1.53 V vs RHE. Strikingly, when the black films were further investigated for HER LSV (d), the reversibility in film color was visible; however, the catalytic performance slightly poor in comparison to the first HER LSV (at 10 mAcm^{-2}) (b). Interestingly, the overpotentials obtained for OER CV (c) could be directly compared to the first OER CV (see Fig. 2a).

Table S2. The comparison of OER overpotentials of **LiCoBPO** and **NaCoBPO** with other superior selected non-noble catalysts in 1M KOH.

Catalyst	Current density ($mAcm^{-2}$)	Overpotential (mV)	Mass loading ($mgcm^{-2}$)	Reference
LiCoBPO/NF	**10**	**216**	**~3**	**This work**
	100	**324**	**~3**	**This work**
	1000	**470**	**~3**	**This work**
NaCoBPO/NF	**10**	**242**	**~3**	**This work**
	100	**336**	**~3**	**This work**
	1000	**530**	**~3**	**This work**
LiCoBPO/FTO	**10**	**293**	**~1**	**This work**
NaCoBPO/FTO	**10**	**328**	**~1**	**This work**
CoO_x@CN	10	260	~0.42	[30]
Ni_2P/NF	10	240	~3	[31]
$Ni_{12}P_5$/NF	10	260	~3	[31]
MoO_2/NF	10	250	~3.4	[32]
NiFe LDH	10	260	0.04	[33]
MoS_2-Ni_3S_2 HNRs/NF	10	249	13	[34]
Ni_3S_2/NF	10	260	1.6	[35]
CoNi-LDH/Fe-porphyrin	10	264	0.14	[36]
N-G/CoO	10	340	-	[37]
$(Ni, Co)_{0.85}Se$@NiCo-LDH	10	216	6	[38]
FeNi-rGO LDH	10	206	0.25	[39]
MoO_2–CoO–C	10	270	-	[40]
FeOOH/Co/FeOOH	10	245	0.28	[41]
Co-P/Cu	10	345	1	[42]
CoFe-H	10	280	0.02	[43]
NiFe-LDH	10	240	0.19	[44]
Co-Fe-P	10	244	0.42	[45]
$Co_6Mo_6C_2$/NCRGO	10	260	~0.15	[46]
$Ni_xCo_{2x}(OH)_{6x}$@Ni	10	305	4.02	[47]
Co_5Mn-LDH/MWCNT	10	300	~0.28	[48]
CoCr-LDH	10	340	0.255	[49]
Co- Birnessite	10	360	0.28	[50]
Co_3ZnC	10	366	0.34	[51]
CoO_x electrodeposited	10	380	-	[52]
$CoSe_2$	10	320	0.142	[53]
CoMn LDH	10	324	0.22	[54]
$Ni_{1-x}Fe_x$ NC/GC	10	330	~2	[55]
Co_3O_4/ $NiCo_2O_4$ DSNCs	10	340	1	[56]
CoP/Cu	10	345	1	[42]
$Co(OH)_2$	10	325	0.2	[57]
CoO_x	10	325	2	[18]
Co_3O_4/N-rmGO	10	320	~0.17	[58]
$CoFeO_x$	10	360	-	[29]
$NiFeO_x$	10	350	-	[29]
Co phosphide/phosphate	10	300	0.1	[59]
$Ni_xCo_{3-x}O_4$ NWs/Ti	10	370	~3	[60]
Ni-P film	10	344	1.53	[61]
NiCo/NS	10	334	1	[62]
NiCo LDH	10	367	0.23	[63]

Table S3. The comparison of HER overpotentials of **LiCoBPO** and **NaCoBPO** with other highly active selected non-noble catalysts in 1 M KOH

Catalyst	Current density ($mAcm^{-2}$)	Overpotential (mV)	Mass loading ($mgcm^{-2}$)	Reference
LiCoBPO/NF	**-10**	**121**	**~3**	**This work**
	-100	**274**	**~3**	**This work**
	-1000	**391**	**~3**	**This work**
NaCoBPO/NF	**-10**	**207**	**~3**	**This work**
	-100	**307**	**~3**	**This work**
	-1000	**506**	**~3**	**This work**
LiCoBPO/FTO	**-10**	**245**	**~1**	**This work**
NaCoBPO/FTO	**-10**	**298**	**~1**	**This work**
MoS_2	-10	60	-	[64]
MoP	-10	64	3	[65]
$Cu_{95}Ti_5$	-10	60	-	[66]
MoC	-10	77	0.76	[67]
NiMo	-10	70	1	[68]
NiFe	-10	94	-	[69]
CoMo	-10	102	-	[69]
CoS_2	-10	175	1.35	[70]
CoMo	-10	170	454 and 579	[71]
CoS_2	-10	145	1.7	[72]
CoN_x	-10	140	2.8	[73]
Mo_2C	-10	130	0.21	[74]
WS_2	-10	250	0.28	[75]
MoB	-10	225	2	[76]
MoC	-10	130	0.21	[74]
Ni/Mo_2C-PC	-10	179	0.5	[77]
Cu_3P/NF	-10	105	1.2	[78]
Co_9S_8@NOSC-900	-10	235	5	[79]
CoP/CC	-10	209	~1	[80]
CoO_X/CN	-10	232	~0.42	[30]
$NiFe/NiFe_2O_4$/NF	-10	105	-	[81]
MoS_2-Ni_3S_2 HNRs/NF	-10	98	13	[34]
Ni-P electrodeposited	-10	93	1.53	[61]
V/NF	-10	176	0.28	[82]
Ni-P foam	-10	135	0.5	[83]
$NiFeP/Ni_2P$	-10	183	-	[84]
$Ni_xCo_{3-x}O_4/NiCo/NiCoO_x$	-10	155	0.7	[85]
NiNiP/NF	-10	130	10.58	[86]
$Ni_{2.5}Co_{0.5}Fe$/NF	-10	150	0.25	[87]
Ni_2P/GC	-20	250	0.38	[88]
Ni_5P_4 film	-10	180	-	[89]
$NiCo_2S_4$	-20	194	4	[90]
CoNiP/NF	-10	155	1	[91]
Ni_3FeN-NPs	-10	158	0.2	[92]
$Zn_{0.76}Co_{0.24}S$/CoS on Ti	-10	200	1	[93]
Ni_3S_2@Ni	-10	195	-	[94]
NiS/NiF	-10	150	43	[95]
Co_9S_8−Ni_xS_y/NF	-10	163	7	[96]
$Ni_{2.3\%}CoS_2$/CC	-10	150	~1	[97]

Table S4. The comparison of OER and HER overpotentials of BPO's with other benchmark catalysts tested using our three-electrode set-up on FTO and NF in 1 M KOH.

Catalyst	Current density ($mAcm^{-2}$)	OER overpotential (mV)	Current density ($mAcm^{-2}$)	HER overpotential (mV)
		On FTO (loading ~1 $mgcm^{-2}$)		
LiCoBPO	10	293	-10	245
NaCoBPO	10	328	-10	298
$Co_3(PO_4)_2 \cdot 8H_2O$	10	430	-10	358
IrO_2	10	400	-10	430
RuO_2	10	354	-10	-
Pt wire	10	-	-10	42
FTO	10	-	-10	-
		On NF (loading ~3 $mgcm^{-2}$)		
LiCoBPO	10	216	-10	121
	100	324	-100	274
NaCoBPO	10	242	-10	207
	100	336	-100	307
Pt	10	-	-10	42
	100	-	-100	130
IrO_2	10	310	-10	220
	100	430	-100	335
RuO_2	10	292	-10	229
	100	420	-100	370
NF	10	490	-10	260
	100	-	-100	470

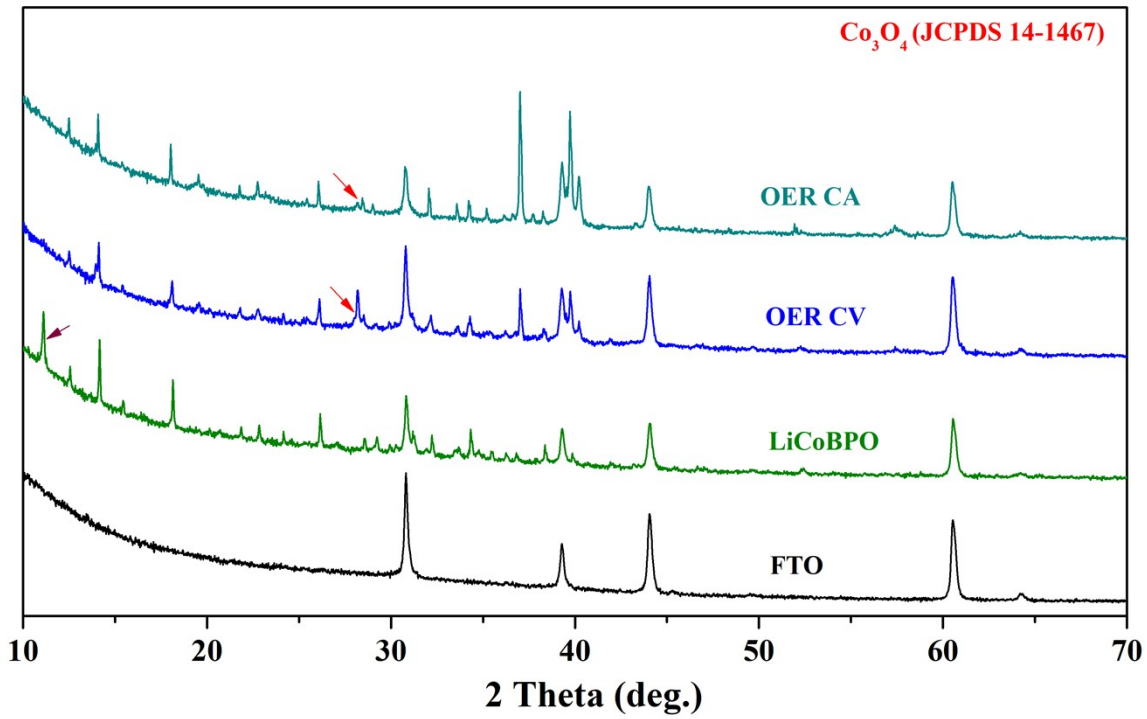

Fig. S23. Grazing Incidence X-ray diffraction patterns (GIXRD) of **LiCoBPO**, post-OER CV and OER CA films along with bare FTO as a reference. Although no major structural changes in the diffraction pattern were observed after OER, the intensity of the reflection at ~11º was decreased in the post OER samples with an unassignable peak at ~28º. The GIXRD result shows that the core of the **LiCoBPO** remained very crystalline under OER conditions whereas the surface of the particles transformed into the amorphous structure (which cannot be identified by PXRD and thus, evidenced by HR-TEM analysis).

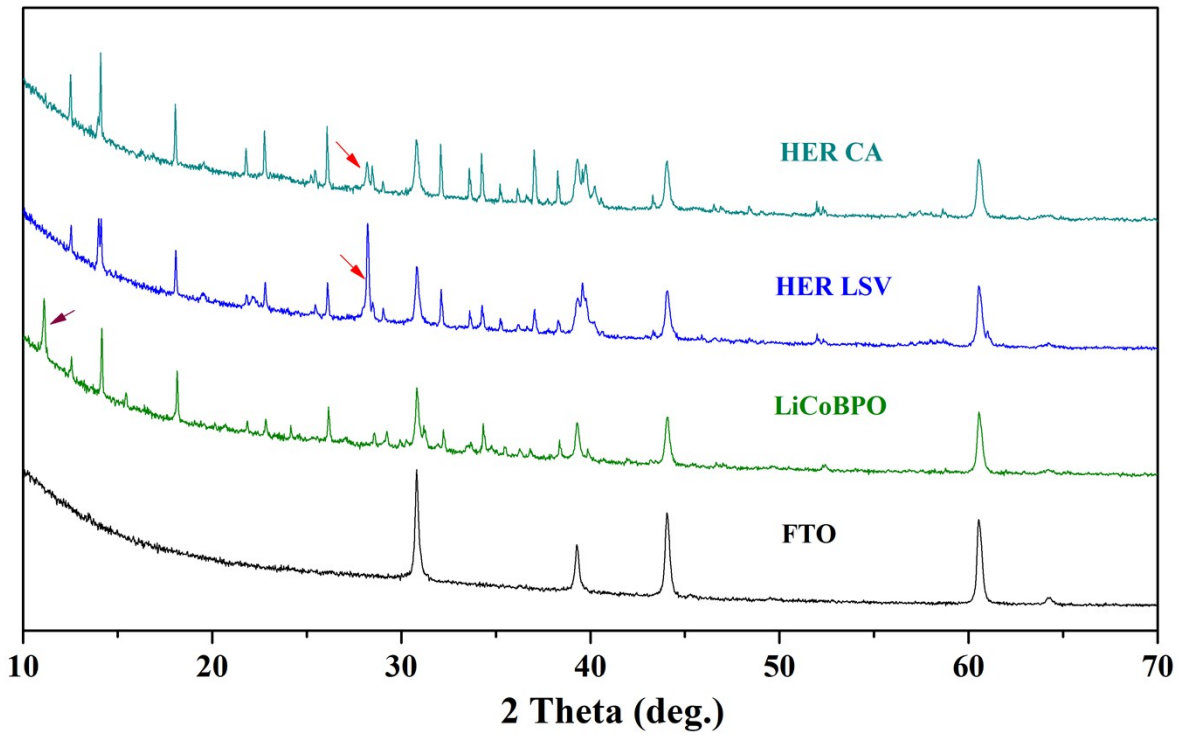

Fig. 24. GIXRD of **LiCoBPO**, post HER CV and HER CA films along with bare FTO as a reference. Similar to OER CA, no major structural changes in the diffraction pattern was observed after OER, apart from the reflection at ~11º which was decreased in the post HER samples with an unassignable peak at ~28º. The GIXRD result shows that the core of the **LiCoBPO** remained very crystalline under HER conditions apart from the surface passivation (as concluded from the HR-TEM analysis).

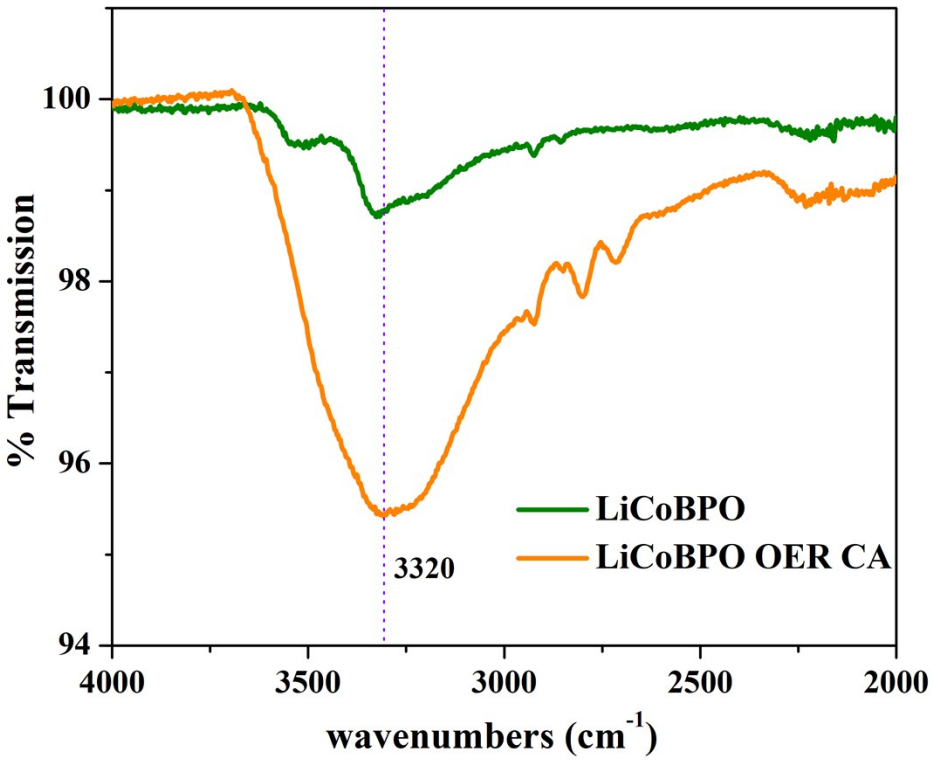

Fig. S25. FT-IR transmission spectrum of as-prepared **LiCoBPO** and the **LiCoBPO** after OER CA experiments. The bands at 3320 cm^{-1} showed that the **LiCoBPO** catalyst after OER is largely hydroxylated.[17]

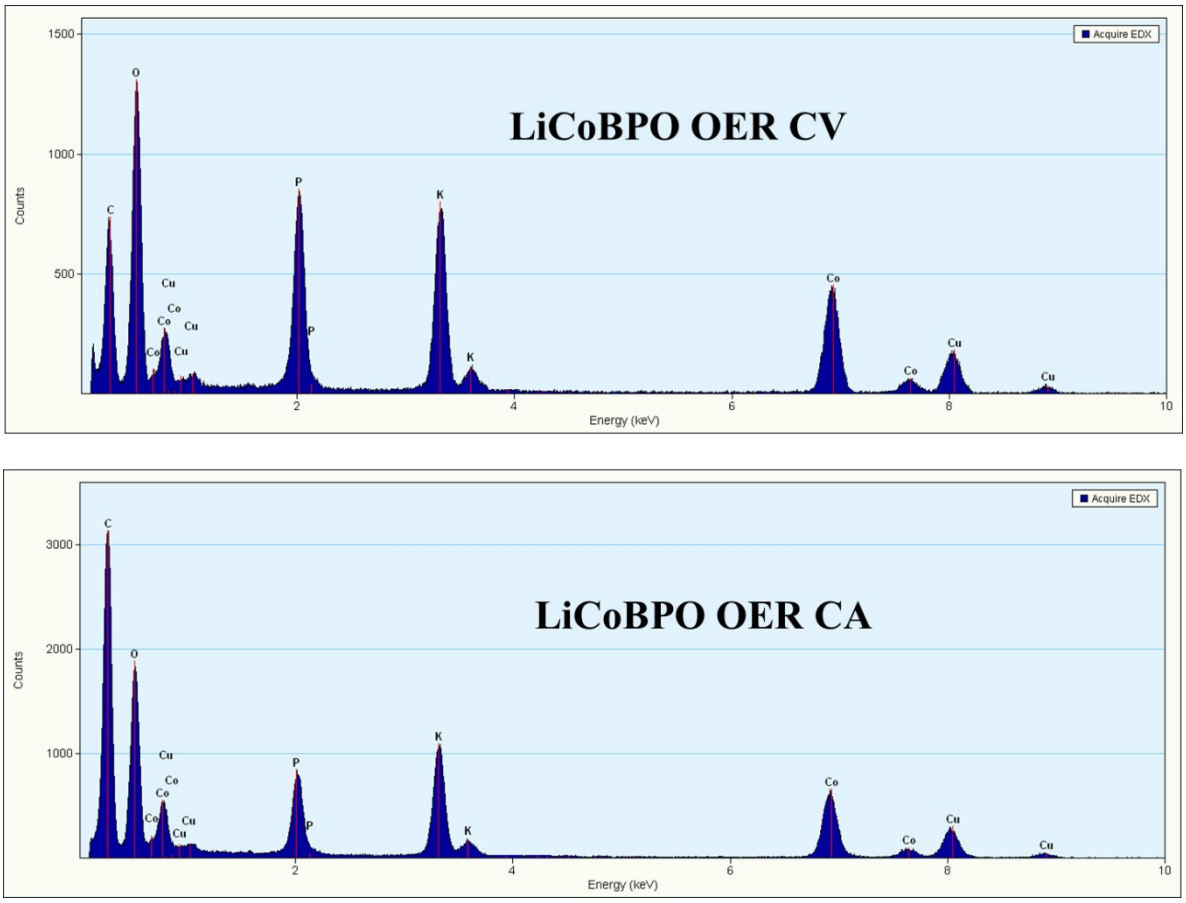

Fig. S26. The presence of cobalt and phosphorous in **LiCoBPO** after OER CA measurements were determined by the EDX analysis. The appearance of peaks for copper is due to the TEM grid (carbon film on 300 mesh Cu-grid) and the potassium is from the used electrolyte under electrochemical conditions.

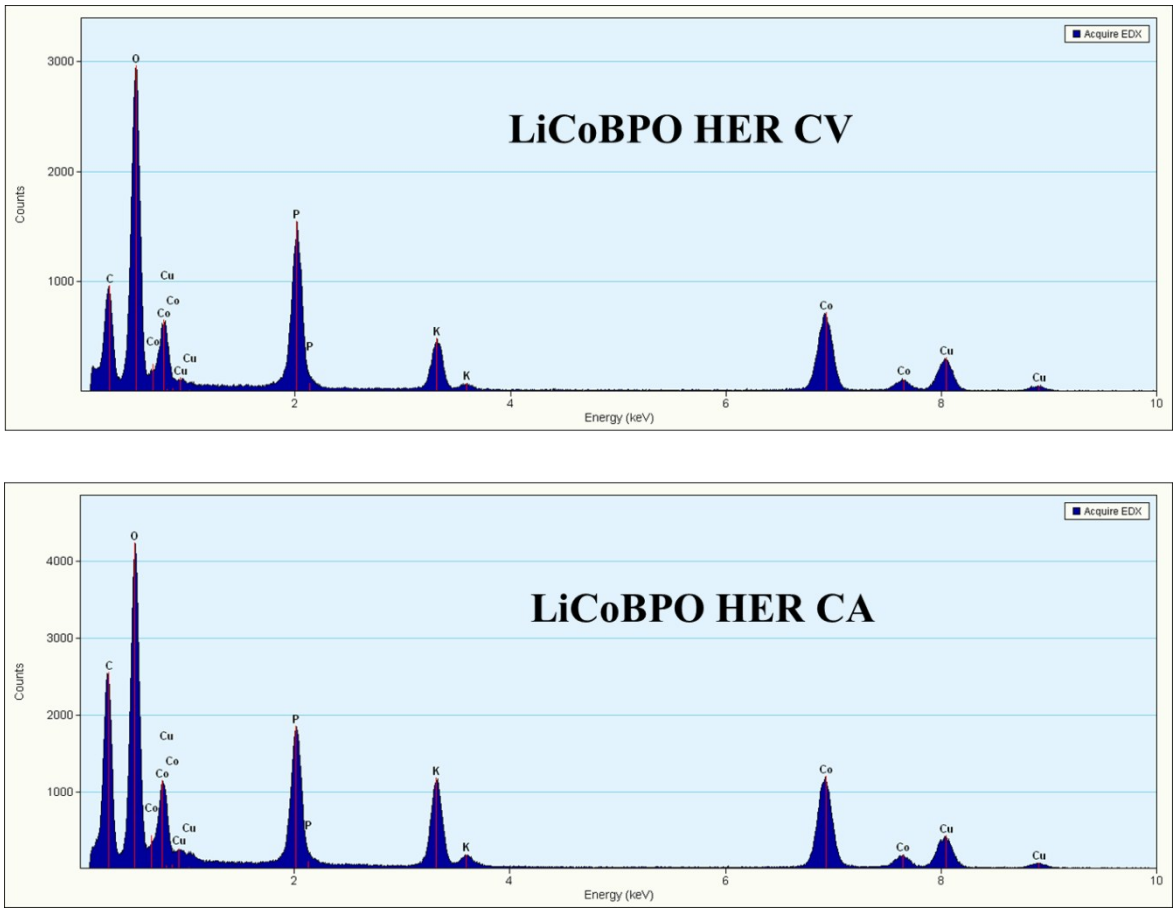

Fig. S27. The presence of cobalt and phosphorous in **LiCoBPO** after HER CA measurements were determined by the EDX analysis. The appearance of peaks for copper is due to the TEM grid (carbon film on 300 mesh Cu-grid) and the potassium is from the used electrolyte under electrochemical conditions.

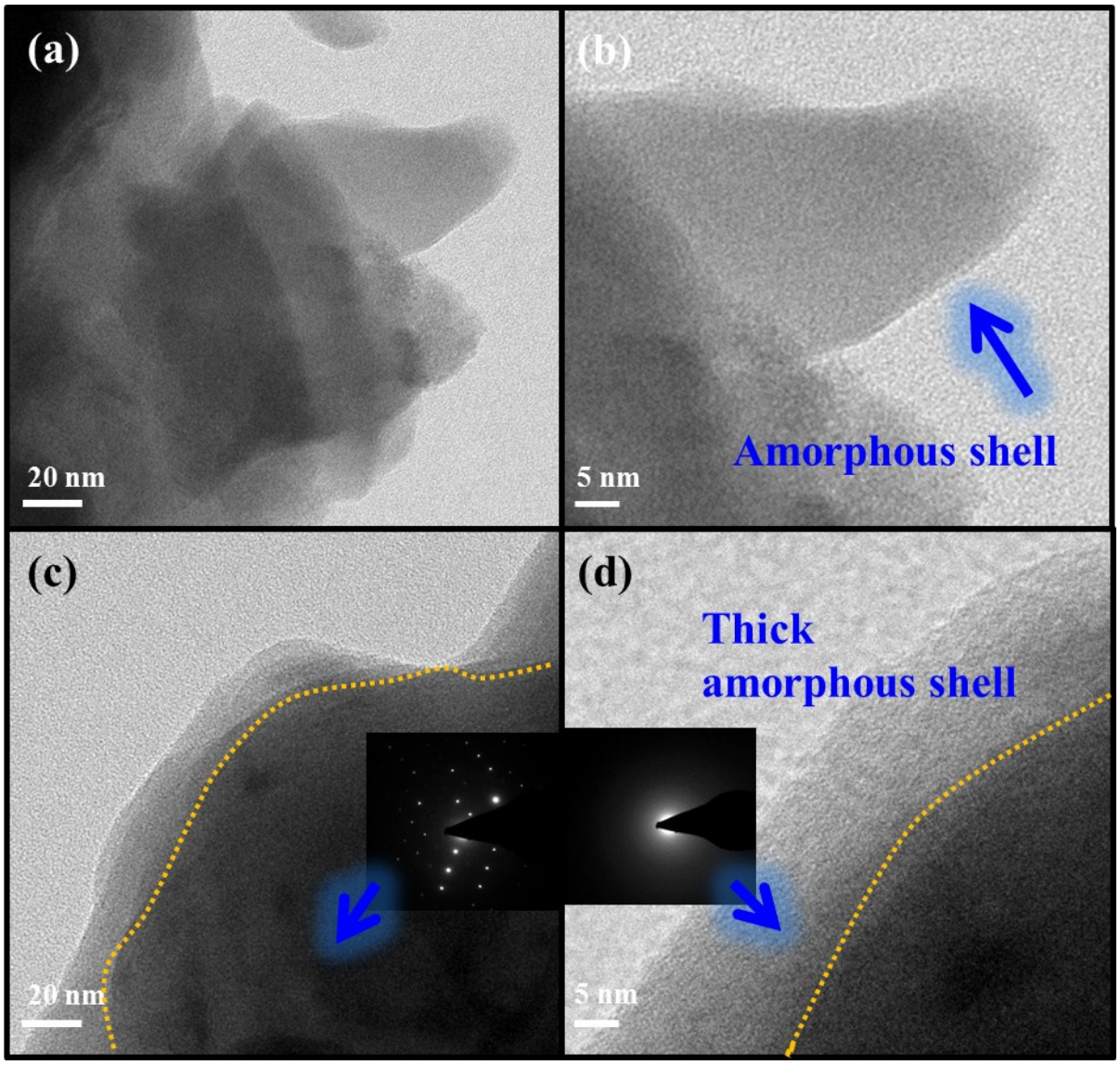

Fig. S28. TEM (20 nm) and HRTEM (5 nm) images of the surface of the thin films of **LiCoBPO** after OER CV (a, b) and after OER CA for 24 h (c, d) measurements in 1 M KOH solution. In the case of OER CV, the modification is very limited that means a very thin amorphous shell (~2 nm) started growing on the surface of the **LiCoBPO** particles indicating the possible formation of hydroxylated phase. After OER CA, a very thick amorphous shell (> 20 nm) was observed indicating a major surface structural change during OER. This type of amorphous shell on the surface of the particles indicating the formation of hydroxylated or oxy-hydroxylated phases has been already discussed in the literature reported transition metal-based catalysts.[17,18,31,98] The corresponding SAED pattern are represented in the inset.

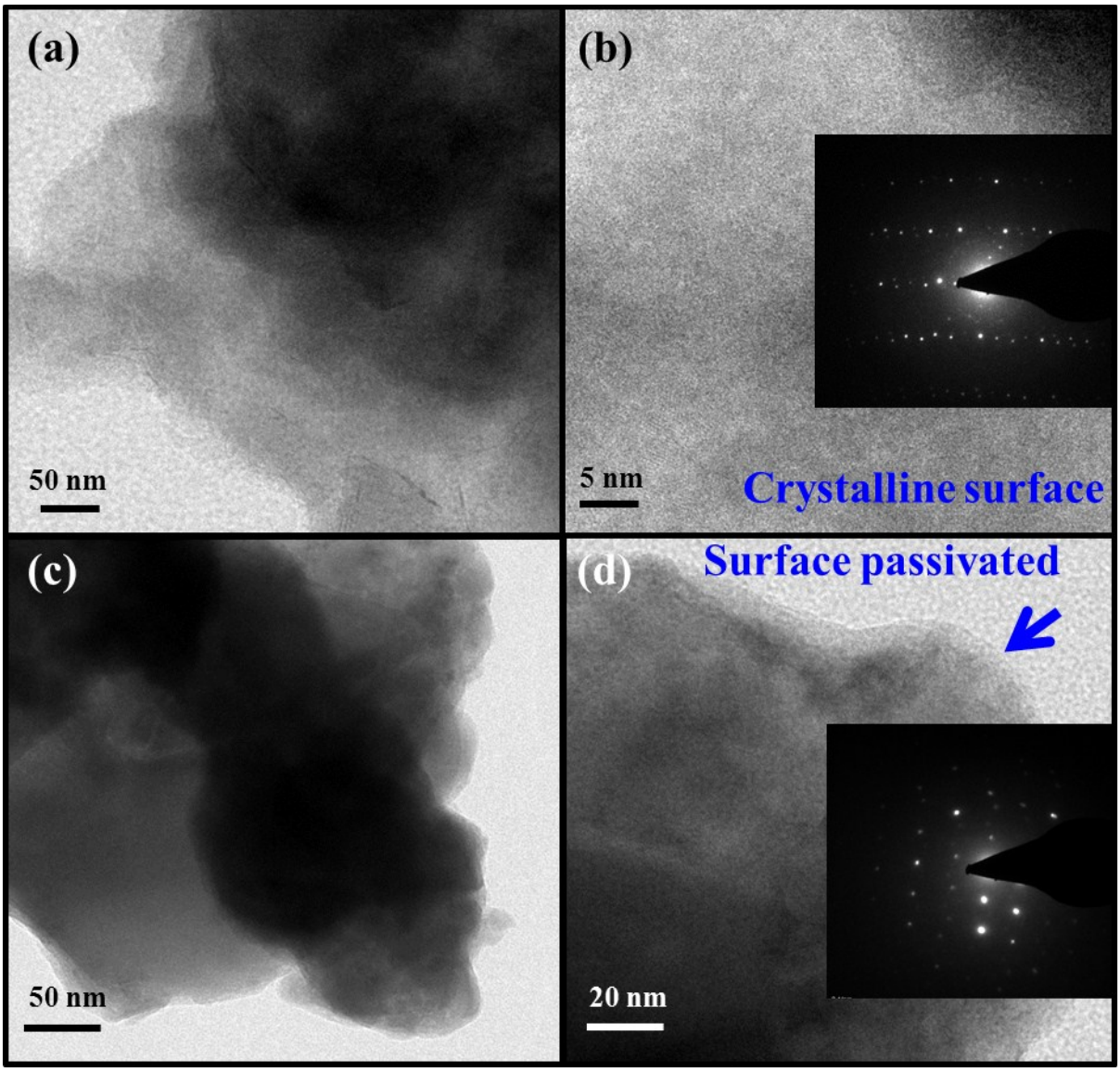

Fig. S29. TEM (50 nm) and HRTEM (5 nm) images of the surface of the thin films of **LiCoBPO** after HER LSV (a, b) and after HER CA for 24 h (c, d) measurements in 1 M KOH solution. In the case of both HER LSV and HER CA, no indication of the surface shell was observed. The particles were well crystalline (see b inset) but the surface was also passivated with CoO_x as shown in (d).[31] The SAED's are shown in the inset.

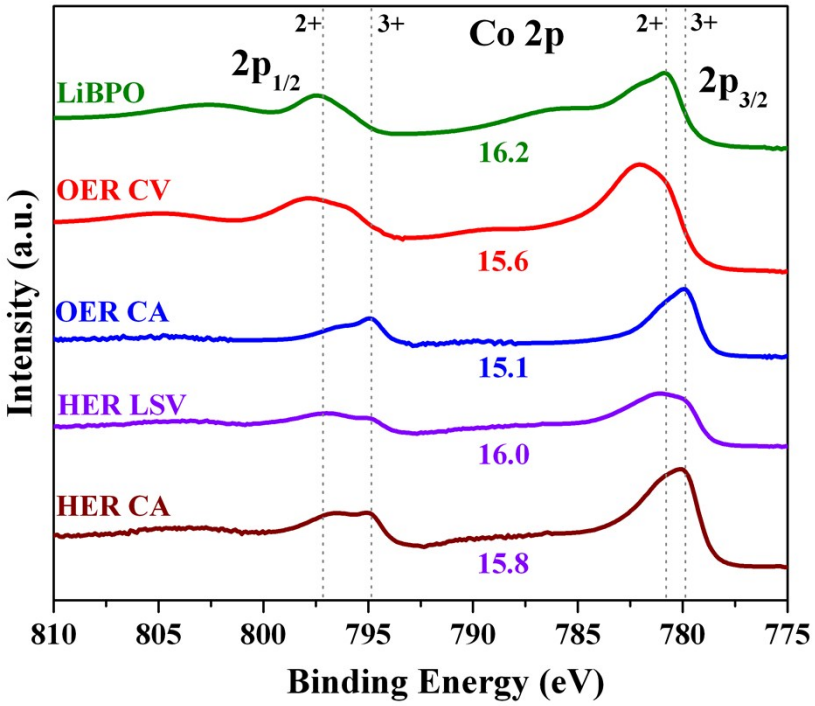

Fig. S30. The difference in the Co $2p_{1/2}$−$2p_{3/2}$ spin−orbit level energy spacing in the XPS spectra of as-prepared **LiCoBPO**, OER CV, OER CA, HER LSV, and HER CA, respectively. For more details, refer to Fig. S31 and S32.

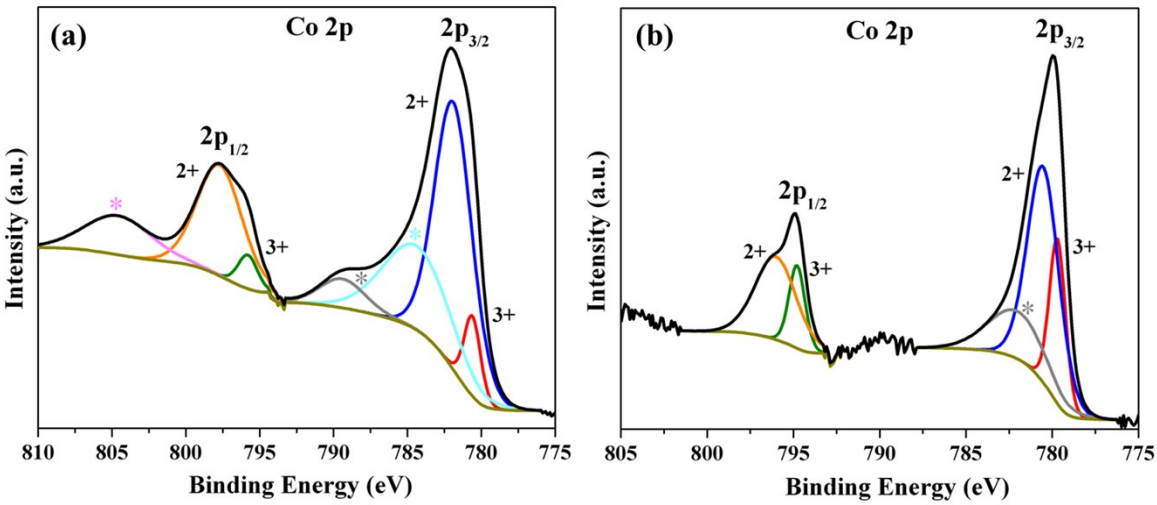

Fig. S31. The Co 2p XPS spectra of **LiCoBPO** after (a) OER CV and (b) OER CA. The Co(II) and Co(III) sites have almost similar 2p binding energies but ultimately, they can be differentiated by the Co $2p_{1/2}$–$2p_{3/2}$ spin–orbit level energy spacing.[12-14] This difference is 16.0 eV for high-spin Co(II) and 15.0 eV for low-spin Co(III). In the case of as-synthesized **LiCoBPO**, the spin–orbit level energy spacing was 16.2 eV indicating that the oxidation state of Co is ~+2. However, after the OER CV, this difference was reduced to 15.6 eV indicating some of the surface oxidation of Co(II) to Co(III). However, after OER CA, the spin–orbit level energy spacing was found to be 15.1 eV that shows almost complete surface oxidation to Co(III). The results obtained here are consistent with the literature reported materials with Co(II) and Co(III).[12,16-18] Interestingly, the surface oxidation of cobalt could also be seen from the HR-TEM results where a thick amorphous shell formation was observed. In both (a) OER CV and (b) OER CA, the $2p_{3/2}$ deconvoluted peaks at binding energy of ~780 and ~781.8 eV could directly be attributed to the Co(III) and Co(II) of the literature reported materials.[12] Similarly, the $2p_{1/2}$ deconvoluted peaks at binding energy of ~795 and ~797 eV are also consistent with the presence of Co(III) and Co(II). In addition, for OER CV, four satellite peaks (represented by *) were also observed at ~785 and ~ 790.5 eV for $2p_{3/2}$ and at 804 eV for $2p_{1/2}$.[99] Furthermore, in the case of OER CA, only a single satellite peak ~782.5 eV was observed which also signifies the surface oxidation of cobalt.[16,17] From detailed analysis and comparing the deconvoluted areas of Co(III) and Co(II) between OER CV and OER CA, it was evident that Co(III) peaks of both $2p_{3/2}$ (red curve) and $2p_{1/2}$ (green curve) were increased after CA while the Co(II) curves (blue and orange curves) were decreased. The resulting percentage of the area of Co 2p region is shown in Table S5.

Table S5. The distribution of the area in the region of Co $2p_{3/2}$ and Co $2p_{1/2}$ XPS with respect to Co(II) and Co(III) oxidation states and satellites for **LiCoBPO** after OER CV and OER-CA experiments.

	Binding Energy (eV)	OER-CV area in %	OER-CA area in %
Co $2P_{3/2}$ Co(III)	~780.5	5.02	15.72
Co $2P_{1/2}$ Co(III)	~795.0	2.48	7.81
Co $2P_{3/2}$ Co(II)	~781.8	37.97	40.34
Co $2P_{1/2}$ Co(II)	~797.5	18.79	20.04
Co 2P Satellite 1	~784.3	21.17	16.09
Co 2P Satellite 2	~789.5	4.93	-
Co 2P Satellite 3	~804.5	9.64	-

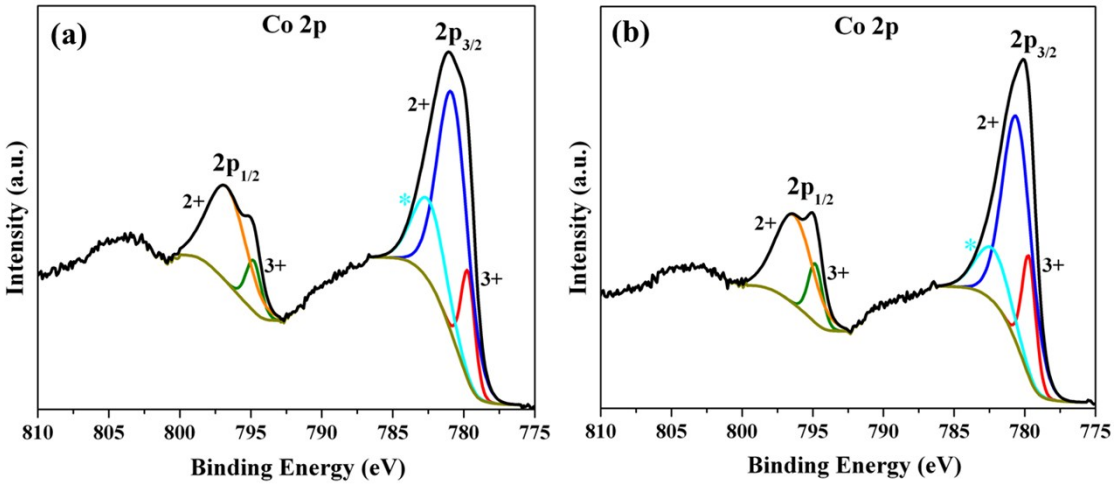

Fig. S32. The Co 2p XPS spectra of **LiCoBPO** after (a) HER LSV and (b) HER CA. As described for the OER, the Co $2p_{1/2}$−$2p_{3/2}$ spin−orbit level energy spacing obtained for HER LSV and HER CA was 16.0 and 15.8 eV, respectively, indicating that there was not much of a difference in the +2 oxidation state of cobalt from the as-synthesized **LiCoBPO.**[12-14] Both in the case of HER LSV and HER CA, the $2p_{3/2}$ deconvoluted peaks at a binding energy of ~781.8 eV suggests that the highest contribution on the surface is from the Co(II) [99]. Similarly, the smallest peaks at ~780 correspond to Co(III) that may have formed from the slight surface passivation. Furthermore, the $2p_{1/2}$ deconvoluted peaks at a binding energy of ~797 eV are also consistent with the presence of Co(II) as major phase and the small peak at ~795 eV corresponds to the surface passivation forming possibly Co(III) species. The results obtained here are consistent with the literature reported examples and can be well corroborated with the presented Table S6.[15,16,18] The values within the Table show that there were no drastic changes in the oxidation state of Co before and after electrochemical measurements. Although, a large amount of metallic Co contribution could be observed in *in-situ* XAS measurement (see later on), however, it was not possible to determine Co(0) in XPS as it is quickly re-oxidizes to Co(II) on the surface of the crystals when exposed to ambient conditions.

Table S6. The distribution of the area in the region of Co $2p_{3/2}$ and Co $2p_{1/2}$ XPS with respect to Co(II) and Co(III) oxidation states and satellites for **LiCoBPO** after HER LSV and HER CA experiments.

	Binding Energy (eV)	HER-LSV area in %	HER-CA area in %
Co $2P_{3/2}$ Co(III)	~ 779.7	9.0	11.89
Co $2P_{1/2}$ Co(III)	~ 794.8	4.77	5.91
Co $2P_{3/2}$ Co(II)	~ 780.5	46.26	46.58
Co $2P_{1/2}$ Co(II)	~ 796.5	22.98	23.14
Co 2P Satellite 1	~ 782.3	16.40	12.50

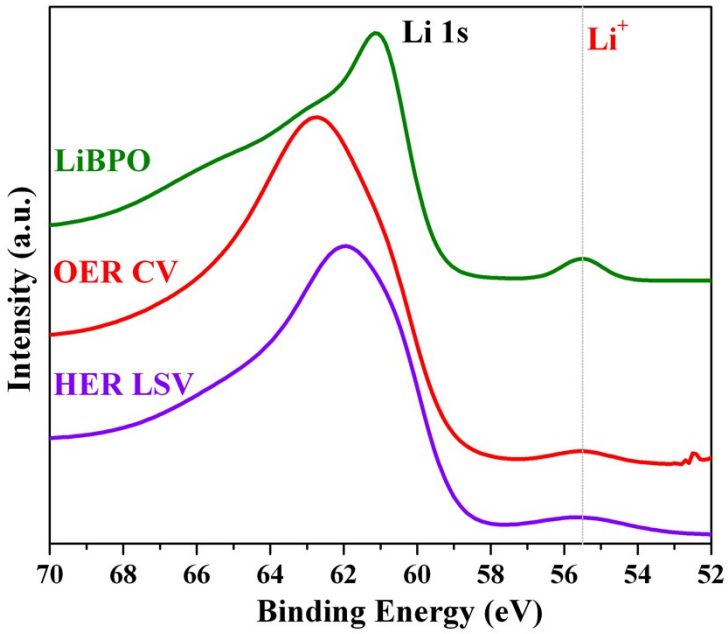

Fig. S33. Typical high-resolution Li 1s XPS spectra of **LiCoBPO** (green), **LiCoBPO** after OER CV (red) and **LiCoBPO** after HER LSV (violet). The Li 1s binding energy peaks at 55.5 eV alongside with the broad Co 3p peak at approximately 62 eV confirms that Li is still present in the surface of the material and values here could be directly compared to other Li^+ compounds.[19,20] Interestingly, after the long-term stability measurement, no lithium was detected on the surface implying a loss of lithium and a complete change of near-surface structure in both HER and OER conditions under applied potentials.

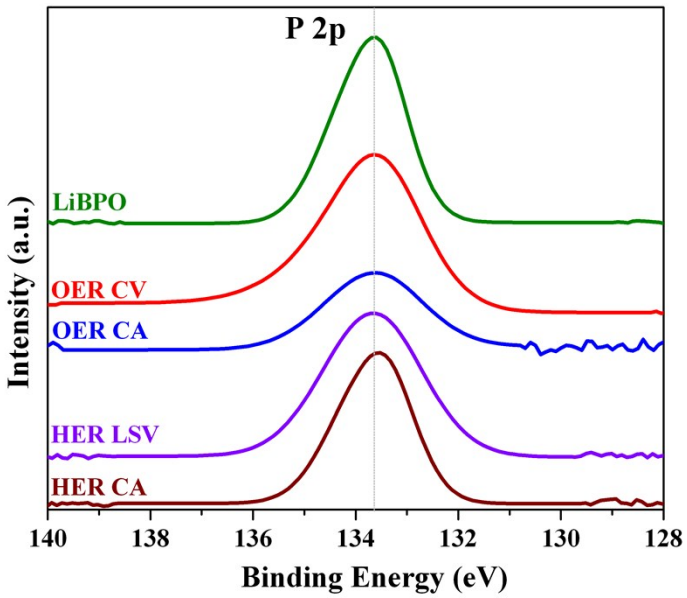

Fig. S34. Typical high-resolution P 2p XPS spectra of **LiCoBPO** after electrochemical OER CV, OER CA, HER LSV, and HER CA. For comparison, the as-prepared **LiCoBPO** is also shown. The peaks at binding energy ~133.8 eV clearly indicated the presence of the only phosphate (PO_4^{3-}) on the surface in all investigated materials of HER and OER, which is in good agreement with the literature reported phosphate materials.[21-23]

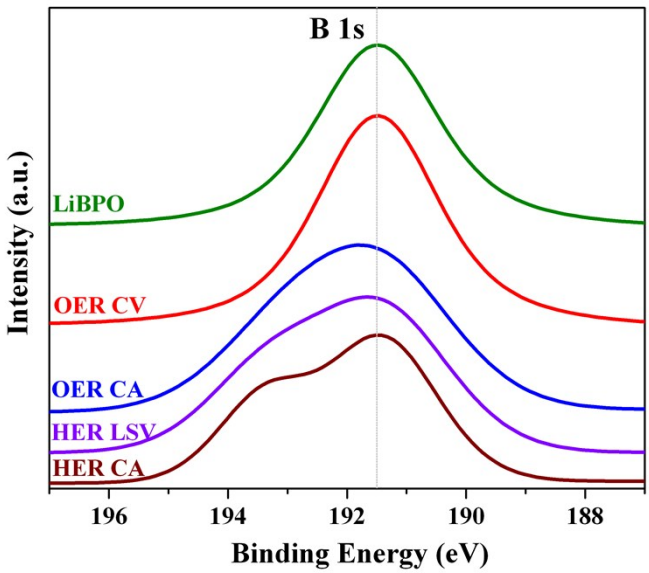

Fig. S35. High-resolution B 1s XPS spectra of **LiCoBPO** after electrochemical OER CV, OER CA, HER LSV, and HER CA. For comparison, the as-prepared **LiCoBPO** is also shown. The B 1s XPS spectra exhibited the main peak at ~191.4 eV in both OER and HER electrochemical conditions corresponding to the structure of boron linked to oxygen atoms with four coordination indicative of B^{3+} (borate) evidencing boron did not change its coordination.[24-26] In CA treated samples, an additional peak starts to appear at 191.4 eV, which could be attributed to the formation of B_2O_3 on the surface.[100,101]

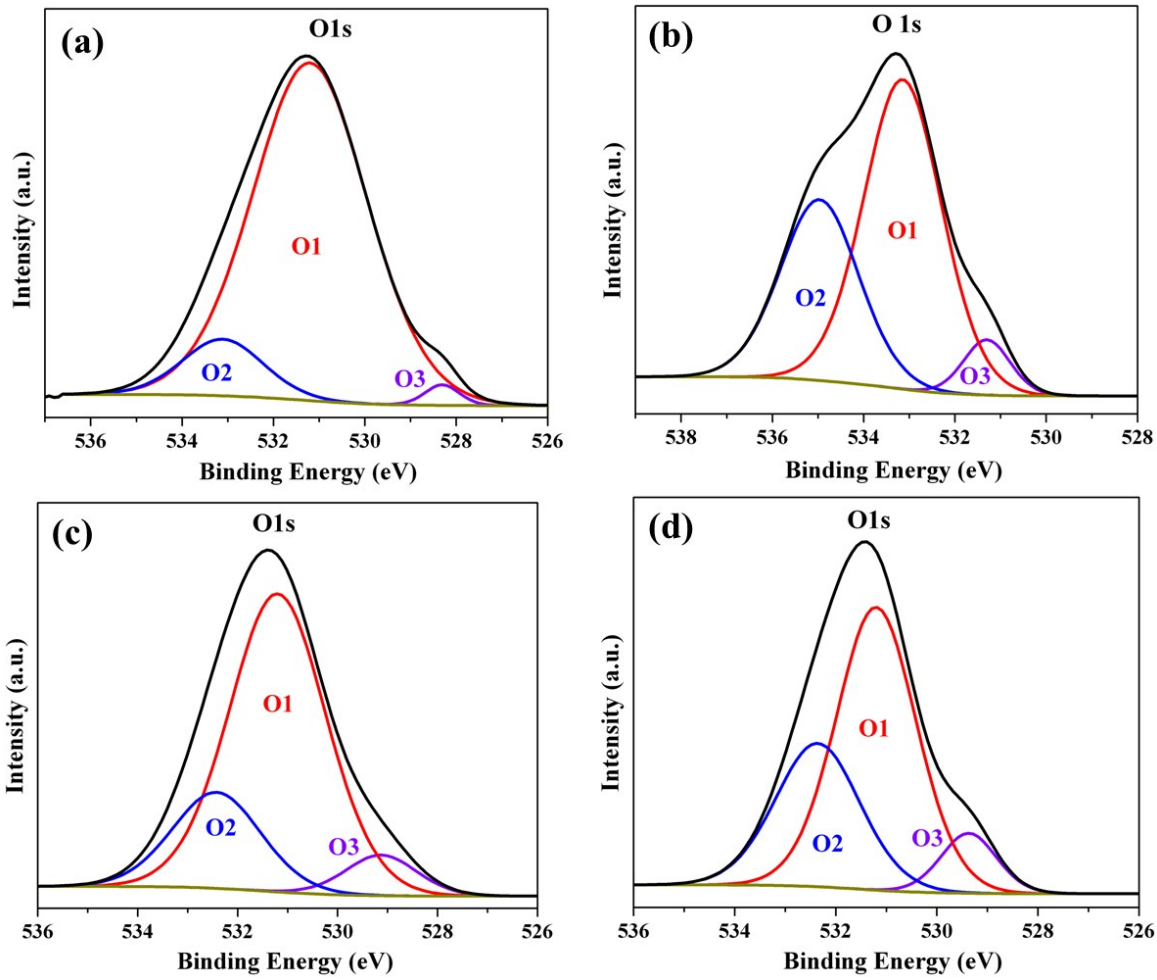

Fig. S36. O 1s XPS spectra of **LiCoBPO** after electrochemical (a) OER CV, (b) OER CA, (c) HER LSV and (d) HER CA. In the case of (a) and (c), the O1s spectrum can be deconvoluted into broad O1, O2, and O3 peaks. The peak at ~531.4 eV (O1) is due to the large dominance of –OH species adsorbed on the surface by surface hydroxides especially after the electrochemical OER treatment. The O2 peak ~532.6 eV (O1) could be assigned to the chemisorbed oxygen or the crystal water associated with the structure. Interestingly, O3 peak between ~529 and ~530 eV indicates the formation of oxides on the surface. However, for (b), O3 peak was shifted towards higher binding energies suggesting the formed metal oxides further hydroxylates under CA conditions in strongly alkaline media. The values obtained here can be easily matched with similar literature reported materials such as phosphates, borates and oxides.[16,18,21,26,99,102]

Table S7. Averaged results of the four-point probe resistivity measurement of the as-synthesized **LiCoBPO** and **NaCoBPO** as well as the after catalytic experiments. Although the as-prepared materials were conductive, the resistivity of the **LiCoBPO** films decreased significantly post electrocatalytic OER and HER measurements improved charge transfer through the materials.

Catalyst	**Resistivity (Ω/sq)**
FTO	7.14
LiCoBPO/FTO	2.53×10^{8}
After OER CA	3.78×10^{6}
After HER CA	2.33×10^{6}
NaCoBPO/FTO	4.31×10^{8}

Table S8. Averaged Co oxidation state determined from the bond-valence-sum of **LiCoBPO**.

Compound	Co-oxidation state
Powder	2.04
as deposited	1.83
HER LSV	1.86
HER CA	1.18
OER CV	2.42
OER CA	2.43

Table S9. Simulation of the material after exposure to oxidizing potentials as a linear combination of the as-deposited **LiCoBPO** and CoCat. For simulation were used k^3-weighted experimental spectra in the range 3 to 14 $Å^{-1}$. In the simulation, the simulated spectrum of the as-deposited **LiCoBPO** was used (meaning that not the experimental, but calculated spectrum was used, taking both distances and coordination numbers as determined for the as-deposited **LiCoBPO**; parameters given in Table S11). For the CoCat spectrum, the simulation parameters from the CoCat spectrum were used (Table S12). In addition, a multiple scattering shell for the collinearly aligned three Co atoms connected by di-μ-oxo bridge was used. The distance for this shell was fixed to the doubled short Co-Co distance in the CoCat (2*2.81 Å). The coordination number (N) gives information about the degree of long-range order in the oxide (for an ideal infinite oxide layer it should be equal to 6) and was determined by a simulation. It is shown in the third column of the table. All Debye-Waller factors were fixed to 0.063 Å.

OER	LiCoBPO, %	CoCat, %	Co-Co^{MS} (N)
after CVs	63.0 ± 4.4	37.0 ± 4.4	1.2 ± 0.8
after CA	62.5 ± 4.4	37.5 ± 4.4	1.1 ± 0.7

Table S10. Simulation of the material after exposure to oxidizing potentials as a linear combination of the as-deposited **LiCoBPO**, metallic Co and CoO. For simulation k^3-weighted experimental spectra were used in the range 3 to 14 $Å^{-1}$. In the simulation, the simulated spectrum of the as-deposited **LiCoBPO** was used (parameters in Table S11). For the metallic spectrum, the simulation parameters from the simulation of the experimental metallic Co were used (Table S14). For the CoO, we did not have an experimental spectrum and we used three shells (one Co and two O) with coordination numbers predicted by the crystal structure of CoO and distances varied during the simulations. These parameters are shown in Table S14. All Debye-Waller factors were fixed to 0.063 Å.

HER	LiCoBPO, %	metallic Co, %	CoO, %
after LSVs	83.4 ± 4.5	0.4 ± 2.1	16.2 ± 6.6
after CA	49.7 ± 3.9	38.3 ± 2.0	12.0 ± 5.9

Table S11. Simulation parameters for the **LiCoBPO** powder and as-deposited material. For simulation were used k^3-weighted experimental spectra in the range 3 to 14 Å^{-1}. The errors (grey color) represent the 68% confidence interval of the respective fit parameter (R, absorber-backscatter distance; σ, Debye-Waller parameter), which does not cover systematic errors due to imperfect EXAFS phase functions. The coordination numbers (N, XRD) and distances (R, XRD) calculated according to the crystal structure are shown in blue for comparison and not used in the simulation. The XAS data was collected at 20 K whereas the XRD data was collected at room temperature; this temperature distance is predicted to result in slightly shorter distances in the low-temperature EXAFS data. The Fourier-filtered error factor was calculated using a Fourier filter between 1 and 5 Å resulting in a value of 28.3% for the powder and 21.8% for the as-deposited material. The Debye-Waller factors for all shells were fixed to 0.063 Å.

	Co-O	**Co-P**	**Co-O**	**Co-O**	**Co-O**
N, XRD	6	4	6	4	11
N, powder	5.7	2.3	5.0	4.7	11.6
error	0.6	1.0	2.8	3.9	5.3
N, as deposited	5.2	2.8	3.7	5.7	9.1
error	0.4	0.7	2.0	2.3	5.4
R, powder [Å]	2.08	3.20	3.67	4.10	4.56
error	0.01	0.02	0.04	0.05	0.03
R, as deposited [Å]	2.08	3.27	3.67	4.06	4.62
error	0.01	0.02	0.03	0.03	0.04
R, XRD [Å]	2.10	3.30	3.71	4.11	4.47

Table S12. Simulation parameters for the CoCat spectrum taken from Ref. 9 (Risch et al.). For simulation were used k^3-weighted experimental spectra in the range 3 to 14 Å^{-1}. The errors (grey color) represent the 68% confidence interval of the respective fit parameter (R, absorber-backscatter distance; σ, Debye-Waller parameter). The Fourier-filtered error factor was calculated using a Fourier filter between 1 and 5 Å resulting in a value of 17.5%. The asterisk (*) indicate the parameters fixed during the simulation.

	Co-O	**Co-Co**
N	6*	3.5
error	-	0.5
R [Å]	1.89	2.81*
error	0.01	-
s [Å]	0.060	0.0632*
error	0.007	-

Table S13. Simulation parameters for the spectrum of the metallic Co. For simulation were used k^3-weighted experimental spectra in the range 3 to 14 $Å^{-1}$. The errors (grey color) represent the 68% confidence interval of the respective fit parameter (R, absorber-backscatter distance; σ, Debye-Waller parameter). The Fourier-filtered error factor was calculated using a Fourier filter between 1 and 5 Å resulting in a value of 18.7%. The asterisk (*) indicate the parameters fixed during the simulation (all coordination numbers were fixed to their values predicted by the structure of the metallic Co). The distances (R, XRD) calculated according to the crystal are shown in blue for comparison.

	Co-Co	**Co-Co**	**Co-Co**	**Co-Co**	**Co-Co**
N	12*	6*	2*	18*	18*
R [Å]	2.50	3.54	4.01	4.36	4.86
error	0.00	0.00	0.02	0.00	0.00
R, XRD [Å]	2.50	3.54	4.07	4.34	4.78
s [Å]	0.046	0.036	0.055*	0.058	0.033
error	0.001	0.004	<0.001	0.003	0.003

Table S14. Simulation parameter obtained by the simulation of the **LiCoBPO** exposed to reducing potentials (Table S10) which were assigned to a CoO phase. In the simulation, the coordination numbers (N) of the shells added to represent the CoO phase were fixed to the values corresponding to the crystal structure of CoO (indicated in the table with asterisks, *). The interatomic distances (R) were varied during the simulation. The errors (grey color) represent the 68% confidence interval. The predicted from the CoO structure distances (R, XRD) are shown for a comparison in blue color. The Debye-Waller parameters were all fixed to 0.063 Å.

	Co-O	**Co-Co**	**Co-O**
N	4*	12*	12*
R, XRD [Å]	1.97	3.21	3.78
R [Å]	1.93	3.18	3.75
error	0.05	0.01	0.10

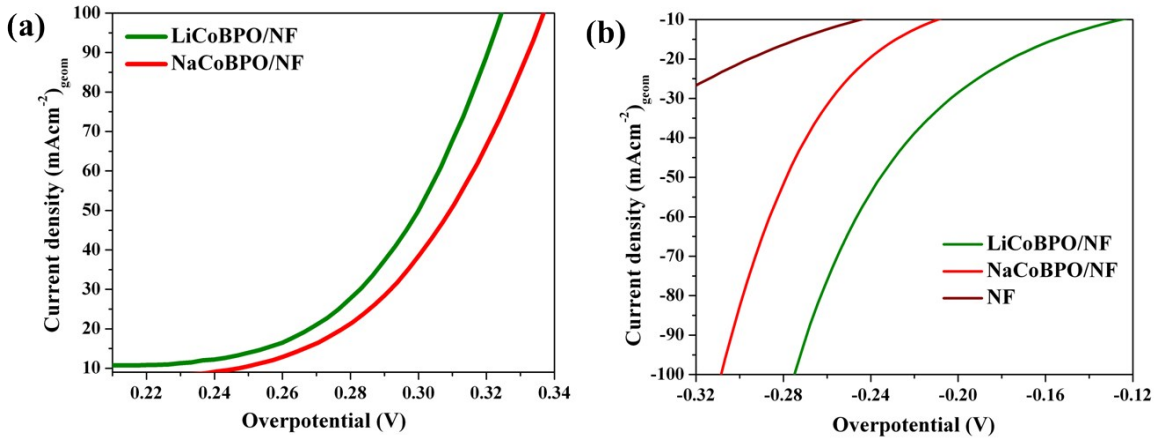

Fig. S37. (a) OER LSV and (b) HER LSV of **LiCoBPO** and **NaCoBPO** deposited on NF at a sweep rate of 5 mV/s of in 1 M KOH electrolyte. The overpotential for the OER (a) was determined to be 216 mV at a current density of 10 $mAcm^{-2}$ for the **LiCoBPO** whereas a slightly higher overpotential of 242 mV was obtained for the **NaCoBPO**. At a current density of 100 $mAcm^{-2}$, the overpotentials were quite close with ~324 and ~336 mV for both **LiCoBPO** and **NaCoBPO**, respectively. The overpotential acquired for HER at -10 $mAcm^{-2}$ was 121 mV for **LiCoBPO** and 207 mV for **NaCoBPO**. Similarly, at -100 $mAcm^{-2}$, the attained overpotential was 274 and 307 mV for **LiCoBPO** and **NaCoBPO**, respectively. The overpotential of **LiCoBPO** in both cases was extremely low in comparison to the transitional metal-based catalyst systems in alkaline media (see Table S3 and S4).

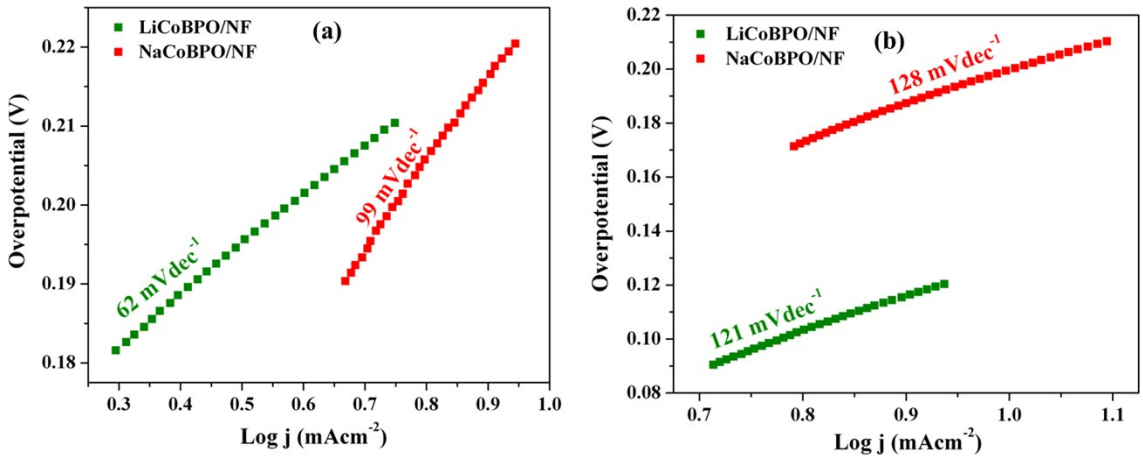

Fig. S38. Tafel slopes derived for (a) OER and (b) HER from the polarization curves at 1 mV/s on NF in 1 M KOH solution. A Tafel slope of 62 $mVdec^{-1}$ was attained for **LiCoBPO** while a higher Tafel slope of 99 $mVdec^{-1}$ was obtained for **NaCoBPO** showing better OER kinetics of **LiCoBPO**. In HER, the Tafel slope of **LiCoBPO** was 121 $mVdec^{-1}$ which was smaller than **NaCoBPO** (128 $mVdec^{-1}$).

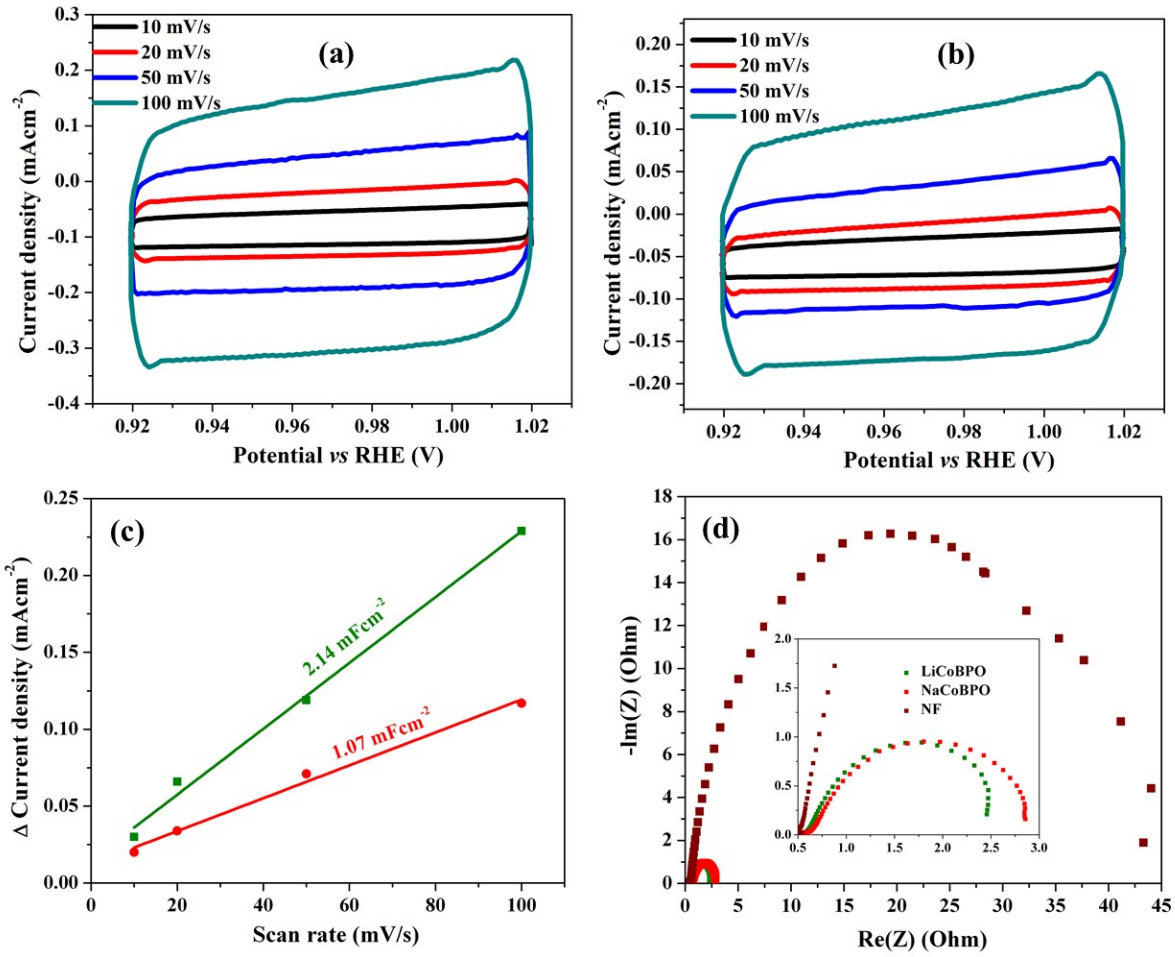

Fig. S39. Electrochemical capacitance measurements for the estimation of the relative ECSA in a non-Faradaic potential range of 0.92 V to 1.02 V vs RHE at different scan rates (10, 20, 50, 100 mV/s) for (a) **LiCoBPO** and (b) **NaCoBPO** on NF in 1 M KOH electrolyte. (c) Estimation of double-layer capacitances (C_{dl}) by plotting the current density variation ($\Delta j = (j_a - j_c)/2$), obtained from the (a) and (b) at 0.97 V vs RHE.[34,103] Nyquist plots (d) obtained from electrochemical impedance spectroscopy (EIS) for **LiCoBPO** and **NaCoBPO**. The spectra were collected with an anodic polarization potential of 1.5 V vs RHE. The inset in (d) is the enlarged EIS curves.[104]

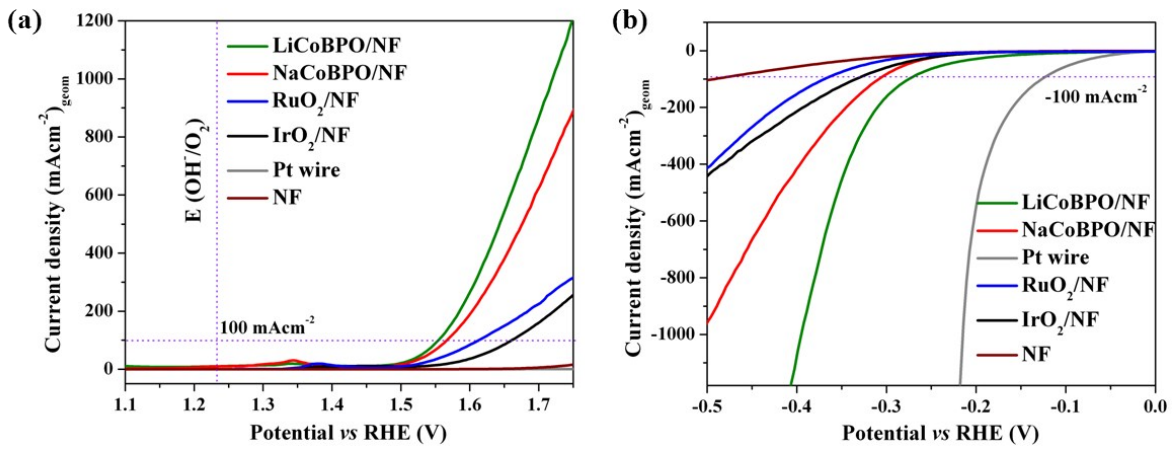

Fig. S40. Comparison of (a) OER LSV and (b) HER LSV of **LiCoBPO** and **NaCoBPO** with noble commercial benchmark on NF at a sweep rate of 5 mV/s of under 1 M KOH electrolyte. In OER, both **LiCoBPO** and **NaCoBPO** surpassed the activity substantially to IrO_2 and the Pt was found to be inactive for OER within the measured range. On the other hand, Pt was extremely active for HER in comparison to **LiCoBPO** and **NaCoBPO** and IrO_2 was clearly less active (see Table S4 for overpotentials).

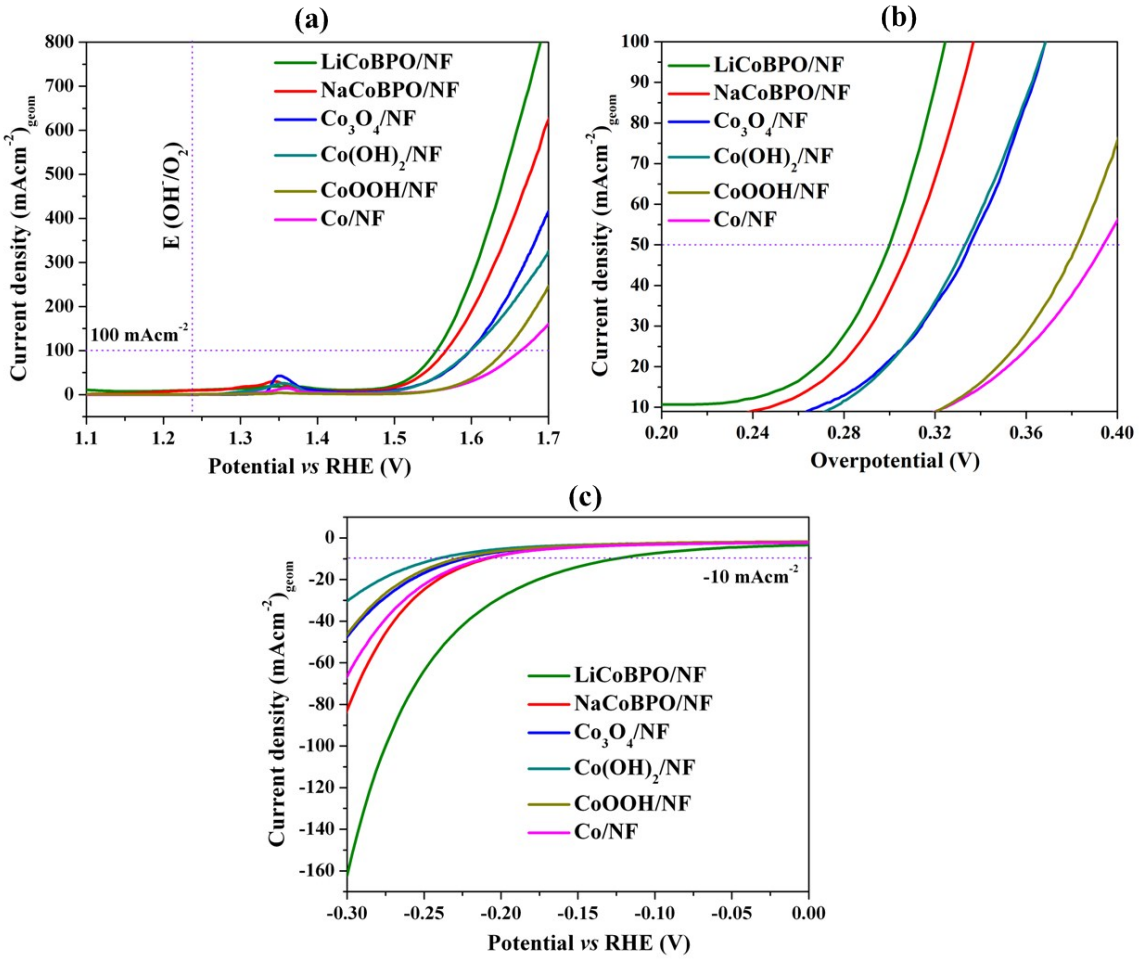

Fig. S41. Comparison of (a, b) OER and (b) HER polarization curves of **LiCoBPO** and **NaCoBPO** with the Co_3O_4, $Co(OH)_2$, CoOOH and the metallic Co catalysts on NF. substrates at a sweep rate 5 mV/s in 1 M KOH electrolyte. On FTO, the overpotential of Co_3O_4, $Co(OH)_2$, CoOOH and Co catalysts at 10 $mAcm^{-2}$ was 360, 380, 400 and 430 mV whereas, for HER, at the same current density the overpotential achieved was 217, 234, 222 and 210 mV, respectively. The attained overpotentials were significantly lower compared to the **LiCoBPO** catalyst (see Table S4).

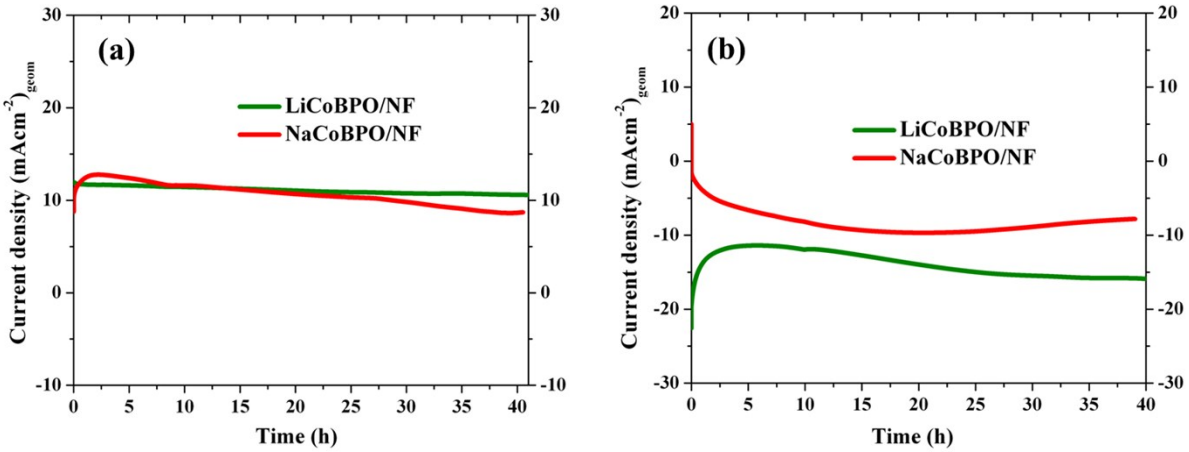

Fig. S42. The chronoamperometric (CA) results of **LiCoBPO** and **NaCoBPO** on NF measured in (a) OER conditions at 1.45 and 1.48 V vs RHE maintaining at 10 $mAcm^{-2}$ in 1 M KOH solution. The **LiCoBPO** catalyst was stable for more than 40 hours but a slight decrease in the **NaCoBPO** was seen. The CA responses of **LiCoBPO** and **NaCoBPO** in (b) HER conditions measured at -0.13 and -0.21 V (at -10 $mAcm^{-2}$) showed activation over time.

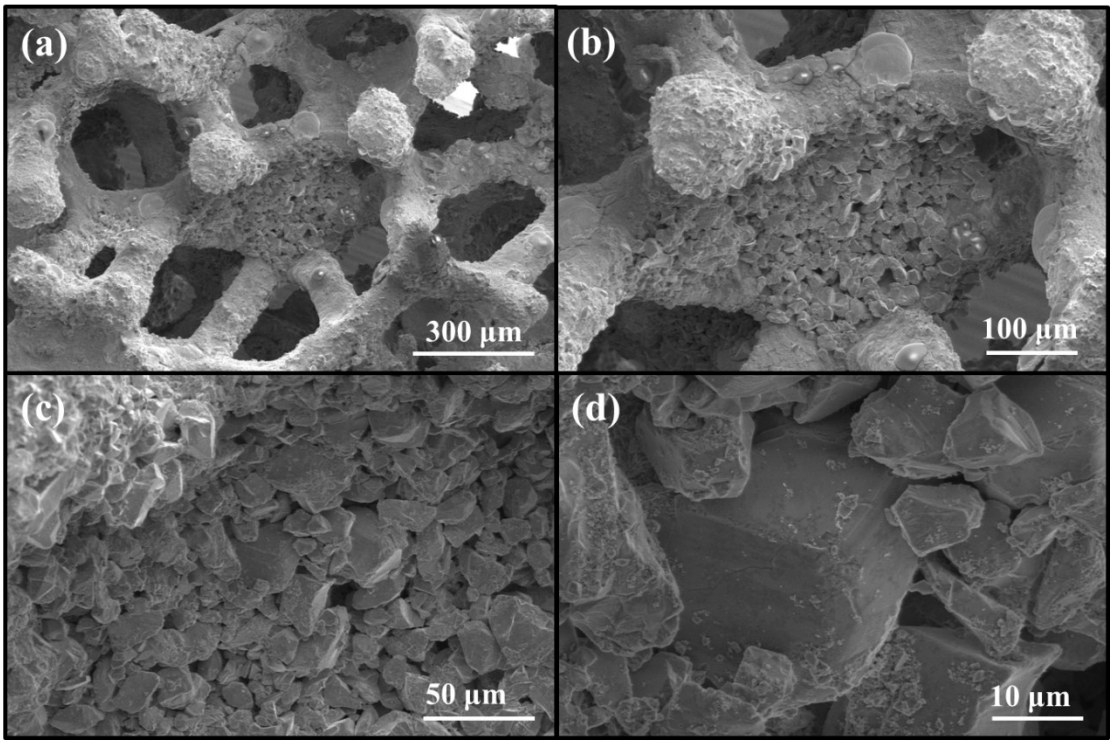

Fig. S43. The SEM images of the as-prepared **LiCoBPO** on NF (a, b) displaying closely packed crystallites at the electrode substrate (c, d).

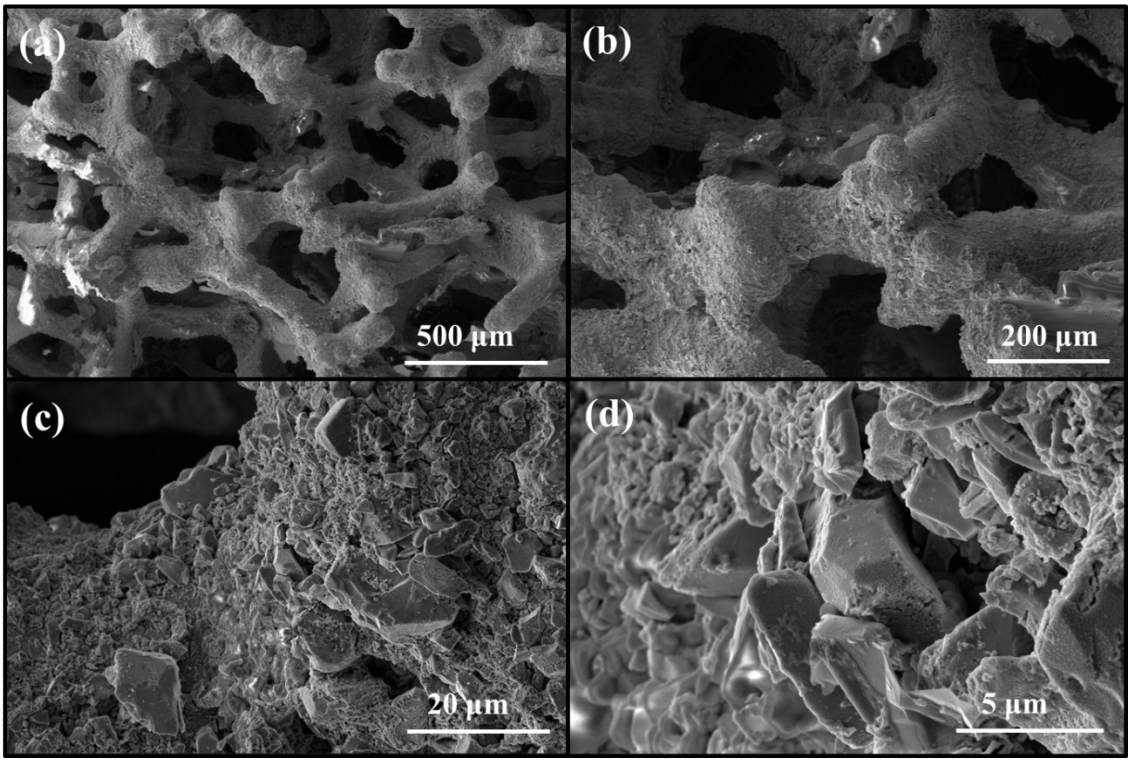

Fig. S44. The SEM images of the **LiCoBPO** on NF after OER CA (a, b). The images showed mostly the surface modified particles (c, d) confirming dramatic changes during electrochemical experiments and are responsible for enhancing the catalytic activity.

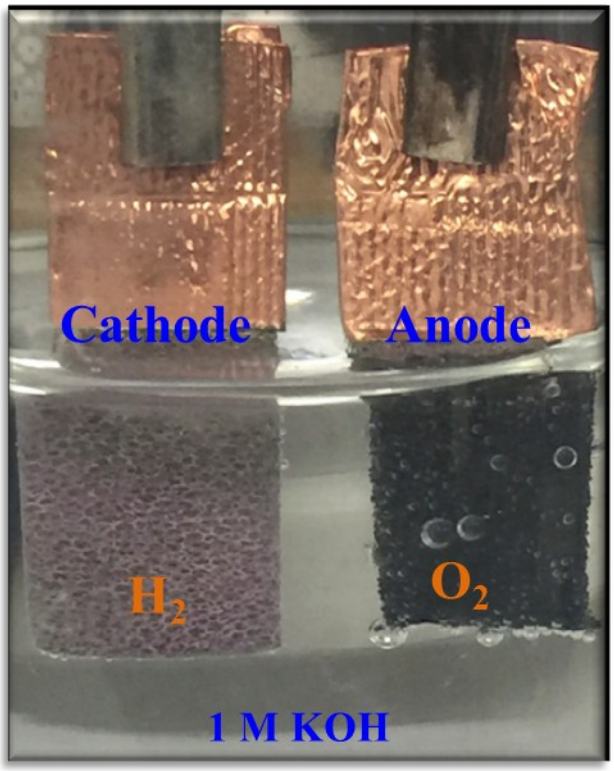

Fig. S45. Overall water-splitting with **LiCoBPO‖LiCoBPO** on nickel foam in 1 M KOH solution with a two-electrode set-up at a potential of 1.53 V (at a current of 10 $mAcm^{-2}$) was applied. Vigorous bubble and gas evolution was observed.

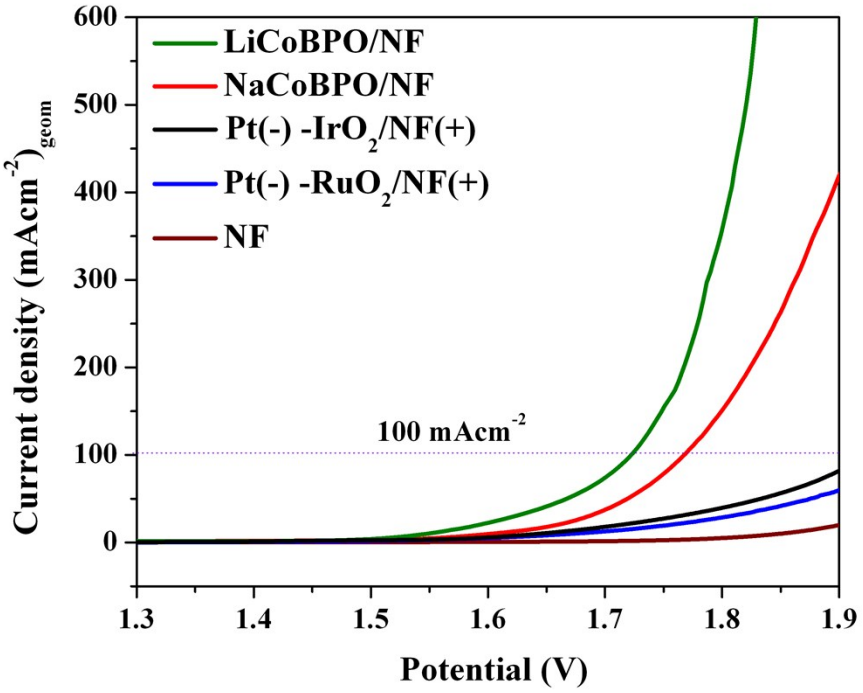

Fig. S46. Comparison of the polarization curves of bare NF‖NF, **LiCoBPO/NF‖LiCoBPO/NF** and **NaCoBPO/NF‖NaCoBPO/NF** with the precious metal-based Pt (-)‖IrO_2/NF(+) and Pt (-)‖RuO_2/NF(+) for overall water-splitting in 1 M KOH at a scan rate of 5 mV/s.

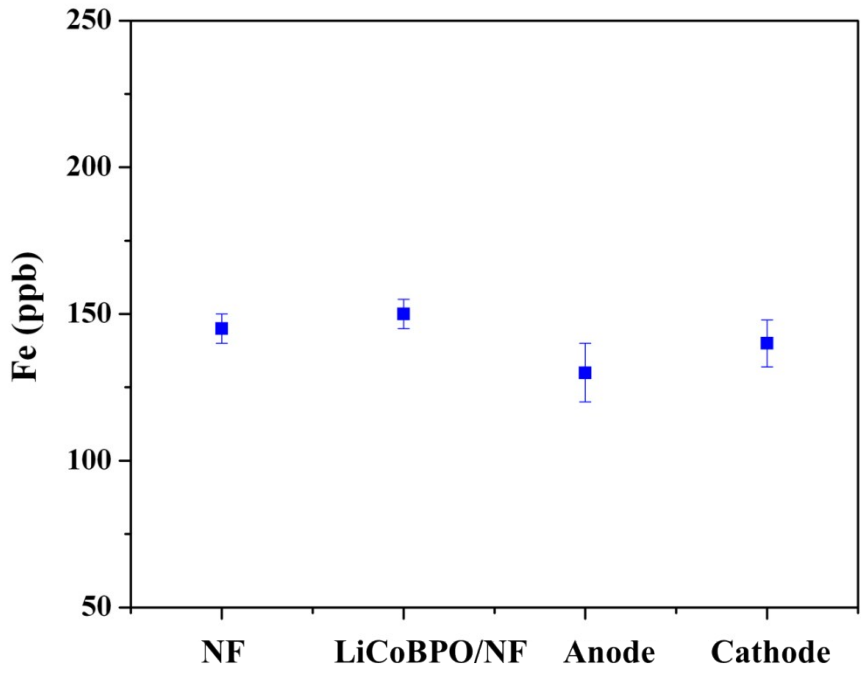

Fig. S47. The determination of Fe impurities from ICP-AES analysis of bare NF, as-prepared **LiCoBPO/NF**, anode and cathode used for overall water-splitting (73 d). The results showed that the amount Fe present in the NF was almost similar to that the other samples that rule out the substantial contribution of Fe from the 1 M KOH electrolyte.

Table S15. ICP-AES analysis of the anode and the cathode after 73 days of electrolysis to determine the compositional changes of **LiCoBPO**. The significant loss of B and P along with the Li shows that major structural modification (CoOOH) takes place at the surface. This can also be correlated to the gradual increase in current density in the CA experiment.

	Theoretical Ratio (Co : B : P : Li)	**Ratio by ICP (Co : B : P : Li)**
LiCoBPO	1 : 1 : 2 : 1	1.0 : 1.02 : 2.0 : 0.98
LiCoBPO/Anode	-	1.0 : 0.55 : 0.85 : 0.06
LiCoBPO/Cathode	-	1.0 : 0.80 : 0.20 : 0.06

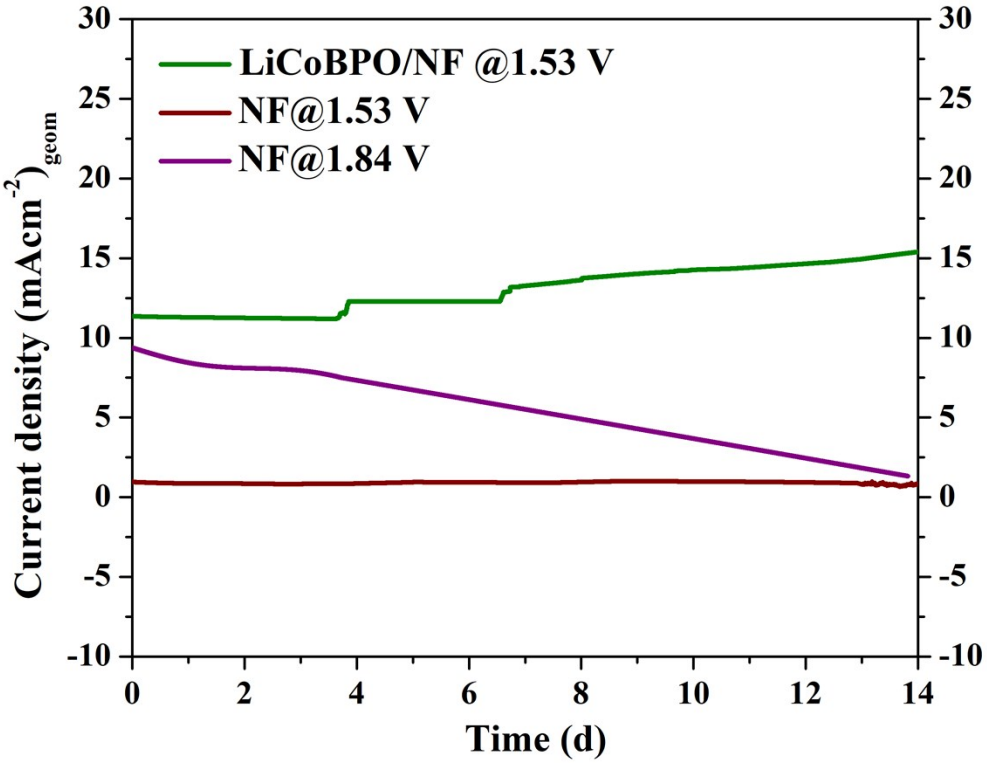

Fig. S48. To rule out the possible influence or contribution of NF in alkaline overall water-splitting, two-electrode set up was fabricated with (a) bare NF‖NF at a potential of 1.53 V (cell potential of **LiCoBPO** at 10 $mAcm^{-2}$) as well as at 1.84 V (cell potential of NF at 10 $mAcm^{-2}$) and the change in the current was monitored. A continuous decrease in the current density with respect to time was attained in both cases revealing the negligible contribution of NF in overall catalysis in 1 M KOH solution. In addition to this, the ICP-AES of the electrolyte was also measured that showed less than 0.001% of Ni leaching. This further eliminates the incorporation of nickel into the structure as well as the possible formation of $Ni(OH)_2$.

ESI Note 1

Based on the microscopic and spectroscopic results, the increase in current density over time (up to 40 days) during the reaction of overall water-splitting of **LiCoBPO** on NF can be attributed to:

1. Easy separation of low coordinated Li ions from the crystal structure of **LiCoBPO** under strongly alkaline electrochemical conditions forming a vacanted, defected and disordered structure to accelerate catalysis both at cathode and anode.

2. Continuous surface transformation of **LiCoBPO** formation of the Co-rich amorphous shell with growing layer thickness at the anode.

3. A slower detachment of B and P from the structure (see Table S15) to form more vacancies at both at anode and cathode and this accommodates further structural transformations to expose more active sites to facilitate overall water-splitting.

After the 40 days of catalysis, no further increase in current was observed. This means that the **LiCoBPO** allows maximum transformation and reorganization of the structure at the surface of anode and cathode to form highly active Co-rich phase. In addition, the inner core of the catalyst still contains **LiCoBPO** (see Table S15) that signifies the crucial roles of B and P in reorganizing the structure, thereby improving overall water-splitting efficiency.

Calculation of Faradaic efficiency

The Faradaic efficiency (FE) of **LiCoBPO** in 1M KOH towards oxygen and hydrogen evolution reaction was measured in a two-electrode configuration where nickel foam loaded with **LiCoBPO** were used as both cathode and anode in a closed electrochemical cell. The electrolyte and cell were first degassed with Argon for 30 min under stirring. Afterward, the constant current density of 10 $mAcm^{-2}$ was applied for a certain period of time. At the end of electrolysis, the gaseous samples were drawn from the headspace by a gas-tight syringe and analyzed by a GC calibrated for H_2, and O_2. Each injection was repeated at least three times and the average value is presented.

The Faradaic efficiency (FE) is calculated based on:

$$FE(H_2,\%) = \frac{V_{H_2} \times 2 \times F}{V_m \times j \times t} \times 100\%$$

$$FE(O_2,\%) = \frac{V_{O_2} \times 4 \times F}{V_m \times j \times t} \times 100\%$$

V_{H2}, V_{O2} is the evolved volume of hydrogen and oxygen, F is the Faraday constant (96485.33289 C/mol), V_m is the molar volume of the gas, j is the current density (10 $mAcm^{-2}$) and t is the time period of electrolysis.

Table S16: Calculation of Faradaic efficiency

	j /$mAcm^{-2}$	t/ sec	V_{H2}/ mL	V_{O2}/ mL	V_{H2}:V_{O2}	FE (H_2,%)	FE (O_2,%)
LiCoBPO	10	900	1.04	0.51	2:1	99	97
After 73 d	10	900	1.02	0.48	2:1	98	94

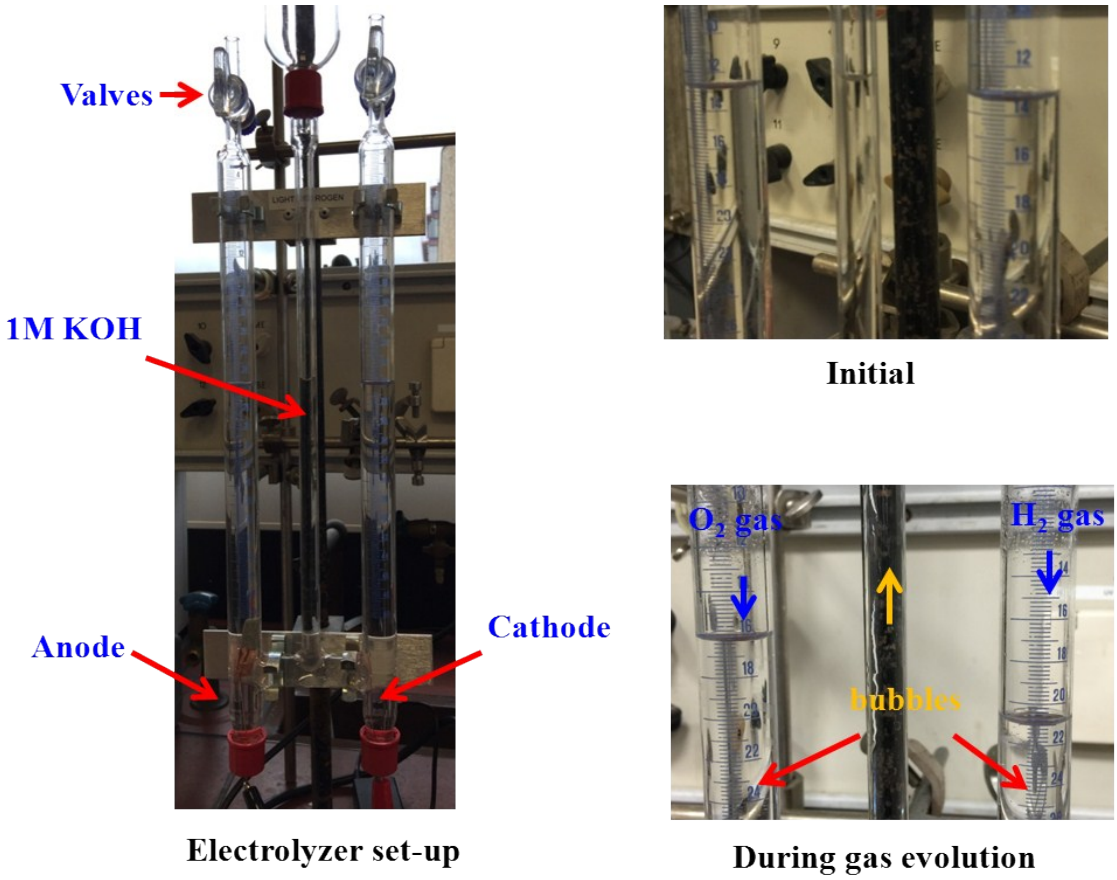

Fig. S49. The electrolysis was performed in a modified two-electrode **LiCoBPO/NF‖LiCoBPO/NF** configuration in 1 M KOH at a constant current density of 10 $mAcm^{-2}$ was carried out in an inverted graduated electrochemical cell to allow collection of H_2 and O_2 separately at atmospheric pressure as shown (left). The initial level of the electrolyte was noted and then the valves were closed (top right). During electrolysis, as a result of evolution and collection of H_2 and O_2 at the upper part of the cell, the level of electrolyte goes down and the change in volume over time is recorded (Figure right). The ratio of volumes of H_2 and O_2 remained almost ~2:1 over the period of electrolysis. The evolved gases H_2 and O_2 were also identified by a gas-chromatograph.

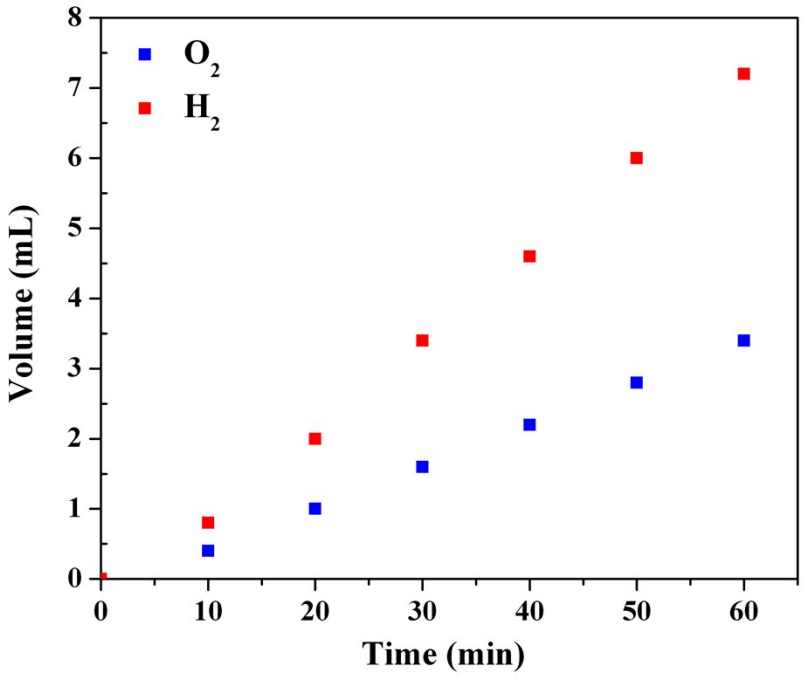

Fig. S50. Graph displaying the volume change as a result of H_2 and O_2 evolution of the experiment carried out in Fig. S49. The ratios of H_2 and O_2 were obtained from the modified two electrodes **LiCoBPO‖LiCoBPO** on NF as both cathode and anode in 1 M KOH solution at a current of 10 mA for 1 h. The obtained ratios of H_2 was approximately twice larger than the O_2 demonstrating the effective selectivity and reactivity of the catalysts.

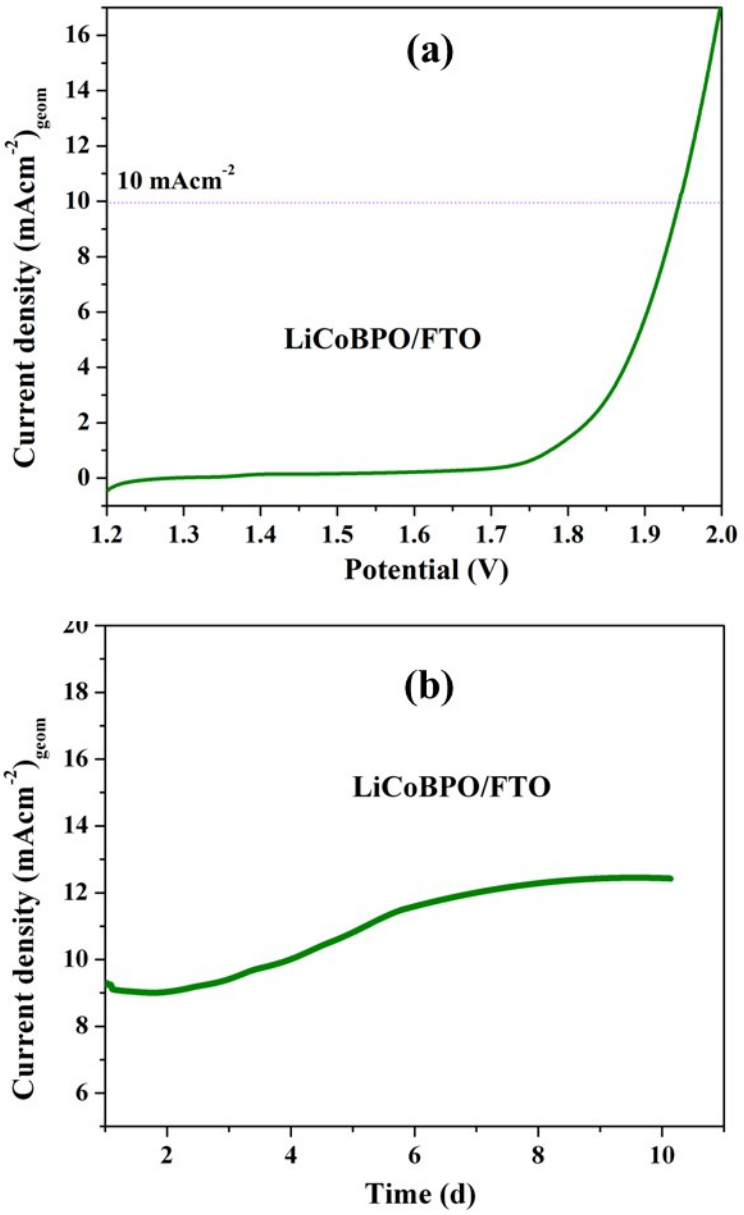

Fig. S51. (a) polarization curve of **LiCoBPO/FTO‖LiCoBPO/FTO** fabricated via a two-electrode setup in 1 M KOH at a scan rate of 5 mV/s displaying a cell potential of 1.94 at a current density of 10 $mAcm^{-2}$ and (b) CA curves at a potential of 1 95 V over 10 days. Similar to **LiCoBPO/NF** substrate, the CA of **LiCoBPO/FTO** substrate which also showed continuous growth in current density over time confirming the fast and easy separation of Li and transformation of the material into a Co-rich surface (see Note 1 for more details) as well as excluding the effect of the electrode substrate.

References:

1. R. Kniep, H. Engelhardt and C. Hauf, *Chem. Mater.* , 1998, **10**, 2930-2934.
2. B. Ewald, Y. X. Huang and R. Kniep, *Z. Anorg. Allg. Chem.*, 2007, **633**, 1517-1540.
3. B. Ewald, Y. Prots, P. Menezes, S. Natarajan, H. Zhang and R. Kniep, *Inorg. Chem.*, 2005, **44**, 6431-6438.
4. P. W. Menezes, S. Hoffmann, Y. Prots and R. Kniep, *Z. Kristallogr.-NCS*, 2009, **224**, 1-2.
5. P. W. Menezes, S. Hoffmann, Y. Prots and R. Kniep, *Z. Kristallogr.-NCS*, 2006, **221**, 251-252.
6. P. W. Menezes, S. Hoffmann, Y. Prots and R. Kniep, *Z. Kristallogr.-NCS*, 2006, **221**, 253-254.
7. P. W. Menezes, Technical University of Dresden, 2009.
8. P. W. Menezes, S. Hoffmann, Y. Prots, W. Schnelle and R. Kniep, *Inorg. Chim. Acta* 2010, **363**, 4299-4306.
9. P. W. Menezes, S. Hoffmann, Y. Prots and R. Kniep, *Z. Kristallogr.-NCS*, 2007, **222**, 1-2.
10. P. W. Menezes, S. Hoffmann, Y. Prots and R. Kniep, *Z. Kristallogr.-NCS*, 2008, **223**, 333-334.
11. R. Kniep, H. G. Will, I. Boy and C. Rohr, *Angew. Chem. Int. Ed.*, 1997, **36**, 1013-1014.
12. M. Oku and K. Hirokawa, *J. Electron Spectros. Relat. Phenom.*, 1976, **8**, 475-481.
13. D. C. Frost, C. A. McDowell and I. S. Woolsey, *Mol. Phys.*, 1974, **27**, 1473-1489.
14. C. A. Kent, J. J. Concepcion, C. J. Dares, D. A. Torelli, A. J. Rieth, A. S. Miller, P. G. Hoertz and T. J. Meyer, *J. Am. Chem. Soc.*, 2013, **135**, 8432-8435.
15. P. W. Menezes, A. Indra, N. R. Sahraie, A. Bergmann, P. Strasser and M. Driess, *ChemSusChem*, 2015, **8**, 164-171.
16. P. W. Menezes, A. Indra, D. Gonzalez-Flores, N. R. Sahraie, I. Zaharieva, M. Schwarze, P. Strasser, H. Dau and M. Driess, *ACS Catal.*, 2015, **5**, 2017-2027.
17. P. W. Menezes, A. Indra, A. Bergmann, P. Chernev, C. Walter, H. Dau, P. Strasser and M. Driess, *J. Mater. Chem. A*, 2016, **4**, 10014-10022.
18. A. Indra, P. W. Menezes, C. Das, C. Gobel, M. Tallarida, D. Schmeisser and M. Driess, *J. Mater. Chem. A*, 2017, **5**, 5171-5177.
19. S. Verdier, L. El Ouatani, R. Dedryvere, F. Bonhomme, P. Biensan and D. Gonbeau, *J. Electrochem. Soc.*, 2007, **154**, A1088-A1099.
20. A. W. Moses, H. G. G. Flores, J. G. Kim and M. A. Langell, *Appl Surf. Sci.*, 2007, **253**, 4782-4791.
21. M. Pramanik, C. L. Li, M. Imura, V. Malgras, Y. M. Kang and Y. Yamauchi, *Small*, 2016, **12**, 1709-1715.
22. F. H. Saadi, A. I. Carim, E. Verlage, J. C. Hemminger, N. S. Lewis and M. P. Soriaga, *J. Phys. Chem. C*, 2014, **118**, 29294-29300.
23. Z. G. Zhao, J. Zhang, Y. Y. Yuan, H. Lv, Y. Y. Tian, D. Wu and Q. W. Li, *Sci. Rep.*, 2013, **3**.
24. S. K. Choi, W. Choi and H. Park, *Phys. Chem. Chem. Phys.*, 2013, **15**, 6499-6507.
25. Y. J. Wang and M. Trenary, *Chem. Mater.* , 1993, **5**, 199-205.

26. X. Y. Sun, Y. X. Ding, B. S. Zhang, R. Huang and D. S. Su, *Chem. Commun.*, 2015, **51**, 9145-9148.
27. P. W. Menezes, A. Indra, O. Levy, K. Kailasam, V. Gutkin, J. Pfrommer and M. Driess, *Chem. Commun.*, 2015, **51**, 5005-5008.
28. Q. Kang, L. Vernisse, R. C. Remsing, A. C. Thenuwara, S. L. Shumlas, I. G. McKendry, M. L. Klein, E. Borguet, M. J. Zdilla and D. R. Strongin, *J. Am. Chem. Soc.*, 2017, **139**, 1863-1870.
29. C. C. L. McCrory, S. H. Jung, J. C. Peters and T. F. Jaramillo, *J. Am. Chem. Soc.*, 2013, **135**, 16977-16987.
30. H. Y. Jin, J. Wang, D. F. Su, Z. Z. Wei, Z. F. Pang and Y. Wang, *J. Am. Chem. Soc.*, 2015, **137**, 2688-2694.
31. P. W. Menezes, A. Indra, C. Das, C. Walter, C. Gobel, V. Gutkin, D. Schmeisser and M. Driess, *ACS Catal.* , 2017, **7**, 103-109.
32. Y. S. Jin, H. T. Wang, J. J. Li, X. Yue, Y. J. Han, P. K. Shen and Y. Cui, *Adv. Mater.*, 2016, **28**, 3785-3790.
33. B. M. Hunter, J. D. Blakemore, M. Deimund, H. B. Gray, J. R. Winkler and A. M. Muller, *J. Am. Chem. Soc.*, 2014, **136**, 13118-13121.
34. Y. Q. Yang, K. Zhang, H. L. Ling, X. Li, H. C. Chan, L. C. Yang and Q. S. Gao, *ACS Catal.* , 2017, **7**, 2357-2366.
35. L. L. Feng, G. T. Yu, Y. Y. Wu, G. D. Li, H. Li, Y. H. Sun, T. Asefa, W. Chen and X. X. Zou, *J. Am. Chem. Soc.*, 2015, **137**, 14023-14026.
36. C. Zhang, J. W. Zhao, L. Zhou, Z. H. Li, M. F. Shao and M. Wei, *J. Mater. Chem. A*, 2016, **4**, 11516-11523.
37. S. Mao, Z. H. Wen, T. Z. Huang, Y. Hou and J. H. Chen, *Energy Environ. Sci.*, 2014, **7**, 609-616.
38. C. Xia, Q. Jiang, C. Zhao, M. N. Hedhili and H. N. Alshareef, *Adv. Mater.*, 2016, **28**, 77-+.
39. X. Long, J. K. Li, S. Xiao, K. Y. Yan, Z. L. Wang, H. N. Chen and S. H. Yang, *Angew. Chem. Int. Ed.*, 2014, **53**, 7584-7588.
40. B. B. Li, Q. Liang, X. J. Yang, Z. D. Cui, S. Z. Qiao, S. L. Zhu, Z. Y. Li and K. Yin, *Nanoscale*, 2015, **7**, 16704-16714.
41. J. X. Feng, H. Xu, Y. T. Dong, S. H. Ye, Y. X. Tong and G. R. Li, *Angew. Chem. Int. Ed.*, 2016, **55**, 3694-3698.
42. N. Jiang, B. You, M. L. Sheng and Y. J. Sun, *Angew. Chem. Int. Ed.*, 2015, **54**, 6251-6254.
43. W. Liu, H. Liu, L. N. Dang, H. X. Zhang, X. L. Wu, B. Yang, Z. J. Li, X. W. Zhang, L. C. Lei and S. Jin, *Adv. Func. Mater.*, 2017, **27**.
44. K. Zhang, W. H. Wang, L. Kuai and B. Y. Geng, *Electrochimi. Acta*, 2017, **225**, 303-309.
45. T. Zhang, J. Du, P. X. Xi and C. L. Xu, *ACS Appl. Mater. Interfaces*, 2017, **9**, 362-370.
46. Y. J. Tang, C. H. Liu, W. Huang, X. L. Wang, L. Z. Dong, S. L. Li and Y. Q. Lan, *ACS Appl. Mater. Interfaces*, 2017, **9**, 16978-16986.
47. Z. Q. Liu, G. F. Chen, P. L. Zhou, N. Li and Y. Z. Su, *J. Power Sources*, 2016, **317**, 1-9.

48. G. Jia, Y. F. Hu, Q. F. Qian, Y. F. Yao, S. Y. Zhang, Z. S. Li and Z. G. Zou, *ACS Appl. Mater. Interfaces*, 2016, **8**, 14527-14534.
49. C. L. Dong, X. T. Yuan, X. Wang, X. Y. Liu, W. J. Dong, R. Q. Wang, Y. H. Duan and F. Q. Huang, *J. Mater. Chem. A*, 2016, **4**, 11292-11298.
50. A. C. Thenuwara, S. L. Shumlas, N. H. Attanayake, Y. V. Aulin, I. G. McKendry, Q. Qiao, Y. M. Zhu, E. Borguet, M. J. Zdilla and D. R. Strongin, *ACS Catal.*, 2016, **6**, 7739-7743.
51. J. W. Su, G. L. Xia, R. Li, Y. Yang, J. T. Chen, R. H. Shi, P. Jiang and Q. W. Chen, *J. Mater. Chem. A*, 2016, **4**, 9204-9212.
52. M. D. Merrill and R. C. Dougherty, *J. Phy. Chem. C*, 2008, **112**, 3655-3666.
53. Y. W. Liu, H. Cheng, M. J. Lyu, S. J. Fan, Q. H. Liu, W. S. Zhang, Y. D. Zhi, C. M. Wang, C. Xiao, S. Q. Wei, B. J. Ye and Y. Xie, *J. Am. Chem. Soc.*, 2014, **136**, 15670-15675.
54. F. Song and X. L. Hu, *J. Am. Chem. Soc.*, 2014, **136**, 16481-16484.
55. X. Zhang, H. M. Xu, X. X. Li, Y. Y. Li, T. B. Yang and Y. Y. Liang, *ACS Catal.*, 2016, **6**, 580-588.
56. H. Hu, B. Y. Guan, B. Y. Xia and X. W. Lou, *J. Am. Chem. Soc.* , 2015, **137**, 5590-5595.
57. P. F. Liu, S. Yang, L. R. Zheng, B. Zhang and H. G. Yang, *J. Mater. Chem. A*, 2016, **4**, 9578-9584.
58. Y. Liang, Y. Li, H. Wang, J. Zhou, J. Wang, T. Regier and H. Dai, *Nat. Mater.*, 2011, **10**, 780-786.
59. Y. Yang, H. L. Fei, G. D. Ruan and J. M. Tour, *Adv. Mater.* , 2015, **27**, 3175-3180.
60. Y. G. Li, P. Hasin and Y. Y. Wu, *Adv. Mater.*, 2010, **22**, 1926-1929.
61. N. Jiang, B. You, M. L. Sheng and Y. J. Sun, *ChemCatChem*, 2016, **8**, 106-112.
62. F. Song and X. L. Hu, *Nat. Commun.*, 2014, **5**, 4477.
63. H. F. Liang, F. Meng, M. Caban-Acevedo, L. S. Li, A. Forticaux, L. C. Xiu, Z. C. Wang and S. Jin, *Nano Lett.*, 2015, **15**, 1421-1427.
64. H. Li, C. Tsai, A. L. Koh, L. L. Cai, A. W. Contryman, A. H. Fragapane, J. H. Zhao, H. S. Han, H. C. Manoharan, F. Abild-Pedersen, J. K. Norskov and X. L. Zheng, *Nat. Mater.*, 2016, **15**, 48-53.
65. J. Kibsgaard and T. F. Jaramillo, *Angew. Chem. Int. Ed.*, 2014, **53**, 14433-14437.
66. Q. Lu, G. S. Hutchings, W. T. Yu, Y. Zhou, R. V. Forest, R. Z. Tao, J. Rosen, B. T. Yonemoto, Z. Y. Cao, H. M. Zheng, J. Q. Xiao, F. Jiao and J. G. G. Chen, *Nat. Commun.*, 2015, **6**, 6567.
67. Z. P. Shi, Y. X. Wang, H. L. Lin, H. B. Zhang, M. K. Shen, S. H. Xie, Y. H. Zhang, Q. S. Gao and Y. Tang, *J. Mater. Chem. A*, 2016, **4**, 6006-6013.
68. J. R. McKone, B. F. Sadtler, C. A. Werlang, N. S. Lewis and H. B. Gray, *ACS Catal.*, 2013, **3**, 166-169.
69. C. C. L. McCrory, S. Jung, I. M. Ferrer, S. M. Chatman, J. C. Peters and T. F. Jaramillo, *J. Am. Chem. Soc.*, 2015, **137**, 4347-4357.
70. Y. J. Sun, C. Liu, D. C. Grauer, J. K. Yano, J. R. Long, P. D. Yang and C. J. Chang, *J. Am. Chem. Soc.*, 2013, **135**, 17699-17702.
71. C. L. Fan, D. L. Piron, A. Sleb and P. Paradis, *J. Electrochem. Soc.*, 1994, **141**, 382-387.

72. M. S. Faber, R. Dziedzic, M. A. Lukowski, N. S. Kaiser, Q. Ding and S. Jin, *J. Am. Chem. Soc.*, 2014, **136**, 10053-10061.
73. H. W. Liang, S. Bruller, R. H. Dong, J. Zhang, X. L. Feng and K. Mullen, *Nat. Commun.*, 2015, **6**, 7992.
74. L. Liao, S. N. Wang, J. J. Xiao, X. J. Bian, Y. H. Zhang, M. D. Scanlon, X. L. Hu, Y. Tang, B. H. Liu and H. H. Girault, *Energy Environ. Sci.*, 2014, **7**, 387-392.
75. D. Voiry, H. Yamaguchi, J. W. Li, R. Silva, D. C. B. Alves, T. Fujita, M. W. Chen, T. Asefa, V. B. Shenoy, G. Eda and M. Chhowalla, *Nat. Mater.* , 2013, **12**, 850-855.
76. H. Vrubel and X. L. Hu, *Angew. Chem. Int. Ed.*, 2012, **51**, 12703-12706.
77. Z. Y. Yu, Y. Duan, M. R. Gao, C. C. Lang, Y. R. Zheng and S. H. Yu, *Chem. Sci.* , 2017, **8**, 968-973.
78. A. Han, H. Y. Zhang, R. H. Yuan, H. X. Ji and P. W. Du, *ACS Appl. Mater. Interfaces*, 2017, **9**, 2240-2248.
79. S. C. Huang, Y. Y. Meng, S. M. He, A. Goswami, Q. L. Wu, J. H. Li, S. F. Tong, T. Asefa and M. M. Wu, *Adv. Func. Mater.*, 2017, **27**.
80. J. Q. Tian, Q. Liu, A. M. Asiri and X. P. Sun, *J. Am. Chem. Soc.*, 2014, **136**, 7587-7590.
81. C. L. Xiao, Y. B. Li, X. Y. Lu and C. Zhao, *Adv. Func. Mater.*, 2016, **26**, 3515-3523.
82. Y. Yu, P. Li, X. F. Wang, W. Y. Gao, Z. X. Shen, Y. N. Zhu, S. L. Yang, W. G. Song and K. J. Ding, *Nanoscale*, 2016, **8**, 10731-10738.
83. X. G. Wang, W. Li, D. H. Xiong and L. F. Liu, *J. Mater. Chem. A*, 2016, **4**, 5639-5646.
84. C. G. Read, J. F. Callejas, C. F. Holder and R. E. Schaak, *ACS Appl. Mater. Interfaces*, 2016, **8**, 12798-12803.
85. X. D. Yan, K. X. Li, L. Lyu, F. Song, J. He, D. M. Niu, L. Liu, X. L. Hu and X. B. Chen, *ACS Appl. Mater. Interfaces*, 2016, **8**, 3208-3214.
86. G. F. Chen, T. Y. Ma, Z. Q. Liu, N. Li, Y. Z. Su, K. Davey and S. Z. Qiao, *Adv. Func. Mater.*, 2016, **26**, 3314-3323.
87. X. L. Zhu, C. Tang, H. F. Wang, B. Q. Li, Q. Zhang, C. Y. Li, C. H. Yang and F. Wei, *J. Mater. Chem. A*, 2016, **4**, 7245-7250.
88. L. G. Feng, H. Vrubel, M. Bensimon and X. L. Hu, *Phys. Chem. Chem. Phys.*, 2014, **16**, 5917-5921.
89. M. Ledendecker, S. K. Calderon, C. Papp, H. P. Steinruck, M. Antonietti and M. Shalom, *Angew. Chem. Int. Ed.*, 2015, **54**, 12361-12365.
90. D. N. Liu, Q. Lu, Y. L. Luo, X. P. Sun and A. M. Asiri, *Nanoscale*, 2015, **7**, 15122-15126.
91. A. Han, H. L. Chen, H. Y. Zhang, Z. J. Sun and P. W. Du, *J. Mater. Chem. A*, 2016, **4**, 10195-10202.
92. X. D. Jia, Y. F. Zhao, G. B. Chen, L. Shang, R. Shi, X. F. Kang, G. I. N. Waterhouse, L. Z. Wu, C. H. Tung and T. R. Zhang, *Adv. Energy Mater.*, 2016, **6**.
93. Y. H. Liang, Q. Liu, Y. L. Luo, X. P. Sun, Y. Q. He and A. M. Asiri, *Electrochim. Acta*, 2016, **190**, 360-364.
94. C. B. Ouyang, X. Wang, C. Wang, X. X. Zhang, J. H. Wu, Z. L. Ma, S. Dou and S. Y. Wang, *Electrochim. Acta*, 2015, **174**, 297-301.
95. W. X. Zhu, X. Y. Yue, W. T. Zhang, S. X. Yu, Y. H. Zhang, J. Wang and J. L. Wang, *Chem. Commun.*, 2016, **52**, 1486-1489.

96. D. Ansovini, C. J. J. Lee, C. S. Chua, L. T. Ong, H. R. Tan, W. R. Webb, R. Raja and Y. F. Lim, *J. Mater. Chem. A*, 2016, **4**, 9744-9749.
97. W. Z. Fang, D. N. Liu, Q. Lu, X. P. Sun and A. M. Asiri, *Electrochem. Commun.*, 2016, **63**, 60-64.
98. A. Indra, P. W. Menezes, N. R. Sahraie, A. Bergmann, C. Das, M. Tallarida, D. Schmeisser, P. Strasser and M. Driess, *J. Am. Chem. Soc.* , 2014, **136**, 17530-17536.
99. S. A. Eliziario, J. M. de Andrade, S. J. G. Lima, C. A. Paskocimas, L. E. B. Soledade, P. Hammer, E. Longo, A. G. Souza and L. M. G. Santos, *Mater. Chem. Phys.*, 2011, **129**, 619-624.
100. D. P. Hashim, N. T. Narayanan, J. M. Romo-Herrera, D. A. Cullen, M. G. Hahm, P. Lezzi, J. R. Suttle, D. Kelkhoff, E. Munoz-Sandoval, S. Ganguli, A. K. Roy, D. J. Smith, R. Vajtai, B. G. Sumpter, V. Meunier, H. Terrones, M. Terrones and P. M. Ajayan, *Sci. Rep.*, 2012, **2**.
101. C. W. Ong, H. Huang, B. Zheng, R. W. M. Kwok, Y. Y. Hui and W. M. Lau, *J. Appl. Phys.*, 2004, **95**, 3527-3534.
102. P. W. Menezes, A. Indra, N. R. Sahraie, A. Bergmann, P. Strasser and M. Driess, *ChemSusChem*, 2015, **8**, 164-171.
103. B. You and Y. J. Sun, *Adv. Energy Mater.*, 2016, **6**, 1502333.
104. L. Yu, H. Q. Zhou, J. Y. Sun, F. Qin, F. Yu, J. M. Bao, Y. Yu, S. Chen and Z. F. Ren, *Energy Environ. Sci.*, 2017, **10**, 1820-1827.